

Lateral meltwater transfer across an Antarctic ice shelf

Rebecca Dell^{1,2}, Neil Arnold¹, Ian Willis¹, Alison Banwell^{3,1}, Andrew Williamson¹,
Hamish Pritchard², and Andrew Orr²

¹Scott Polar Research Institute, Lensfield Road, Cambridge, CB2 1ER, UK

²British Antarctic Survey, High Cross, Madingley Road, Cambridge, CB3 0ET, UK

³Cooperative Institute for Research in Environmental Sciences, University of Colorado
Boulder, Boulder, CO, 80309, USA

copernicus-publications

Correspondence to: Rebecca Dell (rld46@cam.ac.uk)

Abstract

Surface meltwater on ice shelves can exist as slush, it can pond in lakes or crevasses, or it can flow in surface streams and rivers. The collapse of the Larsen B Ice Shelf in 2002 has been attributed to the sudden drainage of ~3000 surface lakes, and has highlighted the potential for surface water to cause ice-shelf instability. Surface meltwater systems have been identified across numerous Antarctic ice shelves, although the extent to which these systems impact ice-shelf instability is poorly constrained. To better understand the role of surface meltwater systems on ice shelves, it is important to track their seasonal development, monitoring the fluctuations in surface water volume and the transfer of water across ice-shelf surfaces. Here, we use Landsat 8 and Sentinel-2 imagery to track surface meltwater across the Nivlisen Ice Shelf in the 2016-2017 melt season. We develop the Fully Automated Supraglacial-Water Tracking algorithm for Ice Shelves (FASTISh) and use it to identify and track the development of 1598 water bodies, which we classify as either circular or linear. The total volume of surface meltwater peaks on 26th January 2017 at $5.5 \times 10^7 \text{ m}^3$. At this time, 63% of the total volume is held within two linear surface meltwater systems, which are up to 27 km long, are orientated along the ice shelf's north-south axis, and follow the surface slope. Over the course of the melt season, they appear to migrate away from the grounding line, while growing in size and enveloping smaller water bodies. This suggests there is large-scale lateral water transfer through the surface meltwater system and the firn pack towards the ice-shelf front during the summer.

1 Introduction

The total mass loss from Antarctica has increased from $40 \pm 9 \text{ Gt/y}$ in 1979–1990 to $252 \pm 26 \text{ Gt/y}$ in 2009–2017, providing a cumulative contribution to sea-level rise of $14.0 \pm 2.0 \text{ mm}$ since 1979 (Rignot et al., 2019). Mass loss from Antarctica will likely increase in the near future due, at least in part, to the shrinkage and thinning of some of its ice shelves (Kuipers Munneke et al., 2014; DeConto and Pollard, 2016; Siegert et al., 2019) and the associated acceleration of inland ice across the grounding lines (Fürst et al., 2016; Gudmundsson et al., 2019). Seven out of 12 ice-shelves that bordered the Antarctic Peninsula have collapsed in the last 50 years (Cook and Vaughan, 2010). One of the most notable events was the

45 February-March 2002 collapse of Larsen B, leading to both an instantaneous and a longer
46 term speedup of the glaciers previously buttressed by the ice shelf (Scambos et al., 2004;
47 Wuite et al., 2015; De Rydt et al., 2015), and resulting in their increased contribution to sea
48 level rise (Rignot et al., 2004).

49
50 The unforeseen catastrophic disintegration of Larsen B highlighted the unpredictable nature
51 of ice-shelf collapse, and prompted a search for the causes of ice-shelf instability. Current
52 understanding of the factors causing ice-shelf instability stems from the very limited number
53 of airborne and satellite observations prior to and following collapse events (e.g. Glasser
54 and Scambos, 2008; Scambos et al. 2009; Banwell et al., 2014, Leeson et al., 2020),
55 numerical modelling (e.g. Vieli et al. 2006, Banwell et al. 2013, Banwell and MacAyeal,
56 2015), and the few in-situ measurements investigating recent and current ice-shelf
57 processes (e.g. Hubbard et al. 2016; Bevan et al., 2017; Banwell et al. 2019). It has been
58 suggested that the chain reaction drainage of ~3000 surface meltwater lakes, which covered
59 5.3% of the total ice-shelf area and had a mean depth of 0.82 m (Banwell et al., 2014), may
60 have triggered the near-instantaneous break-up of Larsen B (Banwell et al., 2013; Robel
61 and Banwell, 2019), highlighting the potential importance of surface hydrology for ice-shelf
62 instability. The formation of these ~3000 surface lakes has been attributed to the saturation
63 of the ice shelf's firn layer, making it impermeable (Kupiers Munneke et al., 2014; Leeson et
64 al., 2020). Given this possible role of surface water on ice-shelf stability, it is important to
65 monitor changes in the area and volume of surface meltwater systems across ice shelves,
66 and compare any trends with those observed at Larsen B prior to its collapse.

67
68 Kingslake et al. (2017) identified numerous pervasive surface meltwater systems across
69 many of Antarctica's ice shelves. Meltwater production is often highest around grounding
70 lines, driven by high net shortwave radiation associated with low albedo blue ice areas, high
71 net longwave radiation around nunataks, and high sensible heat transfer from adiabatic
72 warming of katabatic (Lenaerts et al., 2017) and foehn winds (Bell et al., 2018; Datta et al.,
73 2019). Ice-shelf hydrological systems may then take several forms as meltwater may: (i)
74 form surface streams and flow downslope (e.g. Liston and Winther, 2005; Bell et al. 2017);
75 (ii) collect in surface lakes (e.g. Langley et al. 2016); (iii) percolate into the sub-surface and
76 refreeze (Luckman et al., 2014; Hubbard et al., 2016; Bevan et al., 2017); (iv) percolate into
77 the subsurface and flow laterally (Winther et al., 1996; Liston et al., 1999); or (v) percolate
78 into the subsurface and form sub-surface lakes and reservoirs (e.g. Lenaerts et al. 2017).
79 Despite the identification of pervasive meltwater systems, very little is known about their
80 spatial and temporal evolution, both within and between melt seasons. Furthermore, while
81 surface water ponding and the formation of lakes have been implicated in past ice-shelf
82 collapse (Scambos et al., 2003; Banwell et al., 2013), the formation of surface water streams
83 that route water quickly to the ice-shelf front may not necessarily cause instability but rather
84 mitigate against potential surface meltwater-driven collapse (Bell et al., 2017; Banwell,
85 2017). Thus, whether future projected increased surface melt on ice shelves forms lakes or
86 flows rapidly to the ocean via streams has important implications for future ice-shelf stability
87 and potential collapse. To better understand the behavior of surface meltwater lakes and

88 streams , it is important to investigate their spatial and temporal evolution across entire ice
89 shelves through entire summer melt seasons and over multiple melt seasons.

90
91 In this paper, our objective is to develop a tool that can identify surface meltwater bodies on
92 Antarctic ice shelves and track their evolution over time. We build on the work of Pope et al.
93 (2016) and Selmes et al. (2011, 2013) and especially Williamson et al. (2017; 2018a), who
94 developed and used the FAST algorithm for tracking lakes on the Greenland Ice Sheet
95 (GrIS) using MODIS imagery. More specifically, we have adapted the FASTER algorithm of
96 Williamson, et al. (2018b) and Miles et al. (2017), who adapted the FAST method to track
97 GrIS lakes from the higher resolution Landsat 8 and Sentinel-1 and -2 imagery.

98
99 These previous methods need adapting for application on Antarctic ice shelves for three
100 main reasons. First, to account for the observed differences in the geometry of surface
101 meltwater bodies compared to those on the GrIS. Second, to recognise the marked
102 geometry changes that occur over time on Antarctic ice shelves, including the joining of
103 water bodies and the enveloping of some water bodies by others. Third, to identify the
104 apparent transfer of surface melt water over large distances across ice shelves. In
105 Greenland, the majority of surface water bodies form in surface depressions that result from
106 undulations in the bedrock topography and ice flow (Echelmeyer et al., 1991; Sergienko,
107 2013), and therefore these water bodies evolve in the same location on an inter- and intra-
108 annual basis (Banwell et al., 2014; Bell et al., 2018). By contrast, the location of surface
109 water bodies on Antarctic ice shelves reflects variations in the surface topography, which
110 are controlled by a combination of factors including (i) basal channels formed by ocean
111 melting (Dow et al., 2018), (ii) basal crevassing (McGrath et al., 2012), (iii) the development
112 of ice flow-stripes in the grounding zone (Glasser and Gudmundsson, 2012), and (iv) suture
113 zone depressions (Bell et al., 2017). In Antarctica, these factors result in a wide range of
114 surface water body geometries; from circular forms, to long linear features that can traverse
115 significant distances across an ice shelf, and might therefore have significant implications
116 for the lateral transfer of surface meltwater.

117
118 Here, we advance the work of Williamson, *et al.* (2018b) and Miles *et al.* (2017) to produce
119 'FASTISh', a Fully Automated Supraglacial Lake and Stream Tracking Algorithm for Ice
120 Shelves. We develop the FASTER algorithm for use with Landsat 8 and Sentinel-2 data to
121 make it applicable to Antarctic ice shelves. Such adaptations include: (i) assigning
122 approximate depths to pixels with floating ice cover; (ii) acknowledging the geometric
123 variability of surface water bodies across Antarctica and the impact this variability has on
124 the lateral transfer of surface meltwater by categorising water bodies as either circular or
125 linear; (iii) assigning each water body that is tracked over the melt season to one of four
126 categories (always circular, always linear, simple transitions (from circular to linear or vice
127 versa) and envelopment transitions (where water bodies spread and merge with neighboring
128 circular and linear water bodies to form a new water body, or where a water body splits into
129 smaller circular and linear water bodies) to quantify and illustrate the interaction between
130 individual water bodies as the melt season progresses. We then apply the FASTISh

131 algorithm to the Nivlisen Ice Shelf, Antarctica, for the 2016-2017 melt season; the first full
132 melt season to have data coverage over the ice shelf from both Landsat 8 and Sentinel-2.

133

134 **2 Study Area**

135

136 The Nivlisen Ice Shelf (70.3 °S, 11.3°E), is situated in Dronning Maud Land, East Antarctica,
137 between the Vigrid and Lazarev ice shelves (Fig. 1). It has a surface area of 7,600 km², and
138 is ~ 123 km wide by 92 km long. Ice thickness ranges from 150 m at the calving front to ~
139 700 m towards the ice shelf's grounding line in the southeast, and it exhibits flow velocities
140 of around 20 m a⁻¹ to 130 m a⁻¹ (Horwath et al., 2006). To the southeast of the Nivlisen Ice
141 Shelf, there is a blue ice region maintained by katabatic winds, which extends in a south
142 easterly direction for ~ 100 km (Horwath et al., 2006). This blue ice region is characterised
143 by ablation, and adjoins the exposed bedrock nunatak (called Shirmacheroasen), which is
144 positioned where the ice shelf meets the inland ice (Horwath et al., 2006) (Fig.1). Beyond
145 this blue ice region, towards the north, the ice shelf transitions into an accumulation zone as
146 the firn layer thickens (Horwath et al., 2006). In the 2016-2017 melt season, mean daily
147 near-surface temperatures on the Nivlisen Ice Shelf ranged between ~ -25°C and 2°C, and
148 1.6 % of the study area occupied by a surface water body at least once during this time. The
149 Nivlisen Ice Shelf was selected for this study as: i) pervasive surface meltwater features
150 have previously been identified here in optical satellite imagery, showing evidence of
151 widespread melt ponding in both circular and linear water bodies (Kingslake et al., 2017); ii)
152 these meltwater features have shown significant development over a melt season, as source
153 lakes upstream of the grounding line appeared to drain laterally, rapidly flooding large areas
154 of the ice shelf (Kingslake et al., 2015); and iii) the ice shelf is relatively small, allowing quick
155 and efficient development and application of FASTISH before its use more widely across
156 larger Antarctic ice shelves.

157

158 **3 Methods**

159

160 There are four main components to the FASTISH algorithm: i) delineating water body areas;
161 ii) calculating water body depths and volumes; iii) categorising water bodies as either circular
162 or linear based upon their geometries; iv) tracking individual water bodies and measuring
163 their changing dimensions and geometries over time (Fig.2). These will be discussed in
164 sections 3.2 to 3.5 respectively, once the pre-processing steps applied to the imagery used
165 have been outlined (section 3.1).

166

167 **3.1 Images and Pre-Processing**

168

169 **3.1.1 Landsat 8**

170

171 12 Landsat 8 scenes with minimal cloud cover, from between 1st November 2016 and 24th
172 March 2017, and each partially covering the ice-shelf extent, were identified and
173 downloaded from the USGS Earth Explorer website (<https://earthexplorer.usgs.gov>) (Fig.
174 S1). Each scene was downloaded as a Tier 2 data product, in the form of raw digital numbers
175 (DN). Bands 2 (blue), 3 (green), 4 (red) and 8 (panchromatic) were used for this study (Fig.
176 2). Bands 2, 3, and 4 have a 30 m spatial resolution, and Band 8 has a 15 m spatial

177 resolution. Image scene values were first converted from DN to Top-of-Atmosphere (TOA)
178 reflectance values. Typically, Landsat scenes are converted to TOA reflectance values
179 using a single solar angle over the whole image scene. However, here we correct each pixel
180 for the specific solar illumination angle, based on metadata stored in the .ANG file, and using
181 the ‘Solar and View Angle Generation Algorithm’ provided by NASA
182 (https://landsat.usgs.gov/sites/default/files/documents/LSDS-1928_L8-OLI-TIRS_Solar-View-Angle-Generation_ADD.pdf).
183 Converting from DN to TOA values on a per-pixel basis
184 is imperative when mosaicking and comparing images obtained at high latitudes, **as the
185 solar angle at the time of acquisition can vary significantly across each scene due to the
186 large change in longitude.**

187
188 For each Landsat scene, a cloud mask was generated and downloaded from Google Earth
189 Engine (GEE) using the ‘Simple Cloud Score Algorithm’
190 (ee.Algorithms.Landsat.simpleCloudScore). The simple cloud score algorithm assigns a
191 ‘cloud score’ to every pixel in the image based on the following criteria: (i) brightness in
192 bands 2 (blue), 3 (green), 4 (red); (ii) brightness in just band 2 (blue); (iii) brightness in bands
193 5 (near infrared), 6 (shortwave Infrared 1) and 7 (shortwave infrared 2); and iv) temperature
194 in band 10 (thermal). The algorithm also uses the Normalised Difference Snow Index (NDSI)
195 to distinguish between clouds and snow, which prevents snow from being incorrectly
196 incorporated in the cloud mask. The NDSI was developed by Hall et al. (2001) to distinguish
197 between snow/ice and cumulus clouds and is calculated from the following bands:

$$198 \quad \text{NDSI} = (\text{Blue} - \text{Near Infrared 1}) / (\text{Blue} + \text{Near Infrared 1}) \quad (1)$$

199
200
201 We found the ‘simple cloud score algorithm’ to be the most effective cloud masking method
202 for Landsat 8 images, as it assesses each pixel using multiple criteria, making it more
203 effective than any single band threshold. Prior to implementing the FASTISh algorithm, each
204 Landsat scene and corresponding cloud mask was clipped to the study area extent in
205 ArcGIS using the batch clip process. Clipping each scene to the same extent is required
206 when comparing images through the FASTISh algorithm, as tracking individual features over
207 time requires images with a consistent spatial reference frame to determine the location of
208 each water body. The 12 scenes formed six pairs (Fig. S1), with two scenes per day each
209 covering part of the ice shelf. Each scene pair was mosaicked using ArcGIS’s ‘mosaic to
210 new raster’ tool to produce six images providing near-complete coverage of the ice shelf for
211 six days of the 2016-2017 melt season (Fig. S1). All images were projected into the 1984
212 Stereographic South Pole co-ordinate system (EPSG: 3031).

213 214 **3.1.2 Sentinel-2**

215
216 20 Sentinel-2A level-1C scenes obtained between 1st November 2016 and 31st March 2017
217 with minimal cloud cover were downloaded from the Copernicus Hub web site
218 (<https://scihub.copernicus.eu>) (Fig. S1). Bands 2 (blue), 3 (green), 4 (red), and 11 (short
219 wave infrared (SWIR)) were used. Bands 2, 3, and 4 have a spatial resolution of 10 m, and
220 band 11 a spatial resolution of 20 m. The Sentinel-2 data for all bands were downloaded as

221 TOA reflectance values, and were divided by the 'quantification value' of 10,000 (from
222 metadata), to convert the numbers into values that lie within the zero to one range (Traganos
223 et al., 2018). We applied this conversion to bands 2, 3 and 4 as these are the bands used
224 to identify water and calculate its depth, and their values need to be comparable to the
225 values provided by Landsat 8. Each downloaded scene was clipped, mosaicked to produce
226 images with full coverage of the ice shelf, and then re-projected to the WGS 1984
227 Stereographic South Pole co-ordinate system (EPSG: 3031), in line with the Landsat
228 scenes. As the simple cloud score algorithm had not been adapted for application to S2
229 imagery at the time of writing, we computed a cloud mask for each image using a
230 thresholding approach, whereby pixels were categorised as cloudy if the SWIR band value
231 was $> 10,000$. This threshold was selected through visually assessing the effectiveness of
232 various thresholds against the corresponding RGB scenes. As the resolution of the original
233 SWIR band was 20 m, the resultant cloud masks were resampled using nearest neighbor
234 interpolation to 10 m spatial resolution. On two image dates (14th November 2016 and 25th
235 February 2017), this cloud masking approach was not entirely successful as not all clouds
236 were fully masked. Additional individual masks were manually digitised in ArcGIS to ensure
237 all clouds were masked for these images.

238

239 **3.2 Delineating Water Body Areas**

240

241 Water body areas were determined using the Normalised Difference Water Index for ice
242 ($NDWI_{ice}$), which has been widely used previously to calculate the distribution of surface
243 meltwater features on the GrIS and on Antarctic ice shelves (e.g. Yang and Smith 2013;
244 Moussavi et al., 2016; Koziol et al. 2017; Macdonald et al. 2018; Williamson et al. 2018b;
245 Banwell et al. 2019). It is calculated from the normalised ratio of the blue and red bands as:

246

$$247 \quad NDWI_{ice} = (Blue - Red) / (Blue + Red) \quad (2)$$

248

249 These bands were used because water has high reflectance values in the blue band, and
250 there is a relatively large contrast between ice and water in the red band (Yang and Smith,
251 2013). Studies typically apply a single $NDWI_{ice}$ threshold to an image in order to classify
252 pixels as either 'wet' or 'dry' (e.g. Fitzpatrick et al., 2014; Moussavi et al. 2016; Miles et al.
253 2017). Across both Greenland and Antarctica, most studies have used a relatively high
254 $NDWI_{ice}$ threshold of 0.25 to map 'deep' water bodies on ice (Yang and Smith 2013, Bell et
255 al. 2017, Williamson et al. 2018b). The same approach was applied to the Nivlisen Ice Shelf
256 in this study in order to facilitate the detection of deep water bodies only. This is important
257 because if too much shallow water and slush is detected, identifying and subsequently
258 tracking individual water bodies over time becomes difficult. Having applied a 0.25 $NDWI_{ice}$
259 threshold to each image, the resulting water masks were filtered using a two-dimensional 8-
260 connected threshold (i.e. grouping pixels if they were connected by their edges or corners)
261 to identify each individual water body. Water bodies consisting of ≤ 2 pixels (Landsat 8) and
262 ≤ 18 pixels (Sentinel-2), were removed to ensure only water bodies with an area $\geq 1,800$ m²
263 were assessed further. To ensure that pixels with floating ice cover were still included in the
264 analysis, we then used the 'imfill' function within MATLAB to classify any 'dry' pixels situated

265 within a water body as water.

266

267 **3.3 Water Body Depth Calculations**

268

269 Having identified the extent of water bodies, we use a physically-based approach (Sneed
270 and Hamilton, 2007; Arnold et al., 2014; Banwell et al., 2014, 2019; Pope, 2016; Pope et
271 al., 2016; Williamson et al., 2017, 2018b) based on the original work of Philpot (1989), to
272 calculate pixel water depths. Water depth, z , is calculated from:

273

$$274 \quad z = \frac{[\ln(A_d - R_\infty) - \ln(R_{pix} - R_\infty)]}{g} \quad (3)$$

275

276 where R_{pix} is the satellite-measured pixel reflectance, A_d is the lake-bottom albedo, R_∞ is
277 the reflectance value for optically deep (> 40 m) water, and g is the coefficient associated
278 with the losses made during downward and upwards travel in a water column.

279

280 For the Landsat 8 images, pixel water depths were calculated using TOA reflectance data
281 for both the red and panchromatic bands separately, and then averaging these values to
282 give a single final value (Pope *et al.*, 2016; Williamson *et al.*, 2018b). Pope et al. (2016)
283 show that this approach gives the smallest mean difference (0.0 +/- 1.6m) between
284 spectrally-derived and DEM-derived lake depths. However, it should be noted that owing
285 to the rapid attenuation of red light by a water column, this algorithm is only able to retrieve
286 depths up to a maximum of ~ 5 m (Pope et al., 2016). Furthermore, this method assumes:
287 (i) no wind and waves at the water body surface (ii) little to no dissolved/suspended
288 material within the water body, (iii) no inelastic scattering, and (iv) the water body substrate
289 is parallel to the surface and homogenous (Sneed and Hamilton, 2011).

290

291 In our study, the panchromatic band was first resampled using bilinear interpolation from 15
292 m to 30 m spatial resolution to match the resolution of the red band. For the Sentinel-2
293 images, water body depths were calculated using the TOA reflectance values in the red
294 band only, as there is no equivalent panchromatic band (Williamson *et al.* 2018b). To
295 calculate A_d , the mean reflectance value of the second (Landsat) and sixth (Sentinel) rings
296 of pixels outside of each water body was calculated, following a similar approach used by
297 Arnold et al. (2014) and Banwell et al. (2014). The second or sixth ring of pixels surrounding
298 each lake was used to avoid calculating A_d from slushy areas that border each water body;
299 sixth-pixel rings were used for Sentinel-2 images as these represent the same distance
300 away from the water body as two-pixel rings in Landsat images. In very rare cases, wet
301 pixels within a water body could have a reflectance higher than the calculated A_d value,
302 leading to negative water depths. All such pixels were removed from the area and depth
303 matrix (Fig. 2).

304

305 Values for R_∞ were assessed on an image-by-image basis by taking the minimum
306 reflectance value found over optically deep water (the ocean). For images that did not
307 contain optically deep water, the R_∞ value was set to 0 (Banwell et al., 2019). For Landsat 8

308 imagery we used a g value of 0.7507 for the red band, and 0.3817 for the panchromatic
309 band (Pope *et al.*, 2016), and for Sentinel-2 imagery, we used a value of 0.8304 (Williamson
310 *et al.*, 2018b). Pixels that had a floating ice cover and had been filled (see section 3.2) were
311 assigned the mean depth of their respective water bodies, as it is not possible to calculate
312 the depth of a pixel with an ice cover. Individual water body volumes were calculated by
313 multiplying each pixel area by its calculated water depth, and then summing across the water
314 body. To facilitate comparisons between Landsat 8 and Sentinel-2 data, area and depth
315 arrays generated from Landsat 8 images were then resampled to 10 m spatial resolution
316 using nearest neighbour interpolation.

317

318 **3.4 Classifying Water Body Types**

319

320 Having produced area and depth masks for each date, each identified water body was
321 categorised as either circular or linear based on its solidity (defined as the proportion of
322 pixels of the water body that fall within its convex hull), which was calculated using the
323 'regionprops' function in MATLAB (Banwell *et al.* 2014). Linear water bodies have a solidity
324 score closer to 0 reflecting the smaller proportion of wet pixels within the convex hull due to
325 likely greater concavity of the edges, whereas more circular water bodies have a solidity
326 score closer to 1 due to the larger proportion of wet pixels within the convex hull due to the
327 more convex shape. Here, water bodies with a solidity score ≥ 0.45 were classified as
328 circular, and water bodies with a solidity score < 0.45 were classified as linear. This threshold
329 was selected by visually assessing the masks generated from thresholds ranging between
330 0.42 and 0.49, in increments of 0.01, and selecting the threshold that appears to best
331 distinguish between more circular and more linear water bodies (Fig. 3).

332

333 **3.5 Tracking Water Bodies**

334

335 A 3D matrix of all water bodies was compiled, recording the area and volume of each water
336 body over time, as well as whether the water body had a circular or linear geometry (as
337 defined in section 3.4). To track changes in the area and volume of surface meltwater bodies
338 throughout the 2016-2017 melt season, a maximum extent mask was also generated by
339 superimposing the areas of all water bodies identified in each image (Williamson *et al.*,
340 2018b). The maximum extent mask was then used to guide the tracking process. Each
341 individual water body within the maximum extent was prescribed an ID, and changes to the
342 area and volume of each individual water body over time were tracked within its maximum
343 extent (Williamson *et al.*, 2018b).

344

345 In addition to tracking changes in the area and volume of each water body, the FASTISH
346 algorithm also tracks the water body type. From this tracking process, four categories were
347 defined: (i) always circular, (ii) always linear, (iii) 'simple transitions' where a water body is
348 defined as *either* circular or linear and switches between the two categories (either once or
349 more than once, and in either direction), and (iv) 'envelopment transitions' where water
350 bodies spread and merge with neighbouring circular and linear water bodies to form new,
351 larger bodies, or where larger bodies split into smaller circular and linear water bodies. This

352 final category allows us to track the development of large surface water bodies across the
353 ice-shelf surface as it identifies smaller water bodies being subsumed by larger water bodies
354 as the melt season progresses.

355

356 **3.6 Digital Elevation Model**

357

358 To aid interpretations of the tracking results produced by the FASTISh algorithm, we used
359 surface elevation data from the Reference Elevation Model of Antarctica (REMA) database
360 (Howat et al., 2019). Figure 4a shows the REMA Digital Elevation Model (DEM) of the ice
361 shelf at 8 m resolution, produced by mosaicking four, 8 m resolution REMA tiles. In
362 addition, a single 2 m REMA data strip from 31st January 2016 was used to extract the
363 elevation profiles along two tracked water bodies, the Eastern System and the Western
364 System, which are introduced in section 4.2.2.

365

366 **3.7 Regional climate simulation**

367

368 In order to understand how climate variability influences the findings, we analysed results
369 from an atmosphere-only regional climate CORDEX (COordinated Regional climate
370 Downscaling Experiment) simulation of Antarctica using the limited-area configuration of
371 Version 11.1 of the UK Met Office Unified Model (MetUM) for the period 2016-2017. The
372 MetUM is a weather prediction model, which uses a semi-Lagrangian semi-implicit scheme
373 for solving the fully-compressible, non-hydrostatic, deep-atmosphere equations of motion
374 (Walters et al., 2017).

375

376 The setup of the MetUM is similar to that used by Mottram et al. (2020), with the exception
377 that the horizontal resolution for the limited-area Antarctic domain has been increased from
378 50 to 12 km (and consists of 392 × 504 grid points). The Antarctic domain uses the regional
379 atmosphere mid-latitude (RA1M) science configuration (Bush et al., 2019), a rotated
380 latitude-longitude grid in order to ensure that the grid points are evenly spaced, and 70
381 vertical levels up to an altitude of 40 km.

382

383 The required start data and lateral boundary conditions for the Antarctic domain is supplied
384 by a global version run of the MetUM at N320 resolution (640 × 480 grid points, equivalent
385 to a horizontal resolution of 40 km at mid-latitudes), which is itself initialised by ERA-Interim
386 atmospheric reanalysis (Dee et al., 2011). The model is used to provide a series of 12 to 24
387 hr forecasts, provided every 12 hrs, for the period 20151231T1200Z to 20171230T0000Z,
388 i.e. the initial 12 hrs of each forecast is discarded as spin-up, with the remaining part of the
389 forecasts concatenated together to form a continuous time-series for the period November
390 2016 to April 2017. We extracted daily mean and daily maximum near-surface diurnal air
391 temperatures (at a height of 1.5 m above the ground) for the model grid-point immediately
392 to the south of Schirmacheroasen.

393

394 **4 Results**

395

396 **4.1 Spatial Extent and Distribution of Surface Water Bodies**

397

398 The seasonal evolution of meltwater bodies during the 2016-2017 summer is shown in
399 Figure 5. The surface meltwater system transitions from a series of small isolated water

400 bodies clustered towards the grounding line (Fig 5A), to a connected system dominated by
401 two linear water bodies with a length of (a) ~ 20.5 km and (b) ~ 16.9 km that propagate
402 towards the ice-shelf front (Fig 5D).

403
404 For example, on 11th December 2016, few meltwater bodies exist, and they are
405 predominantly clustered within the blue ice region towards the grounding line in the south-
406 west (Fig. 5A). The majority of these water bodies exist as distinct entities, and do not
407 connect to one another. Some meltwater ponds are identified in close proximity to the
408 nunatak. The total volume and area of all surface meltwater bodies on the 11th December is
409 2.8×10^6 m³ and 2.8×10^6 m² respectively (Table 1). The mean water depth is 1.0 m, and
410 the maximum water depth is 3.4 m (Table 1). By 17th December (Fig. 5B), there has been a
411 marked increase in the total volume (3.2×10^7 m³) and area (4.7×10^7 m²) of surface
412 meltwater, held in both circular and linear surface water bodies (Table 1). The mean water
413 depth is 0.7 m and the maximum water depth is 3.1 m (Table 1). Several of the previously
414 isolated ponds have coalesced in some of the main topographic lows. The spatial extent of
415 the surface water bodies extends ~ 2 km further towards the ice-shelf front. In addition, some
416 water bodies have begun to develop towards the eastern edge of the grounding line in a
417 blue ice region.

418
419 A marked shift in the surface meltwater system is identified by 27th December (Fig 5C), as
420 two large linear water bodies have formed along the north-south axis (labelled a and b in
421 Fig. 5C). The Western linear water body (a) is ~ 6.5 km long and ~ 10 km from the Eastern
422 linear water body (b), which is ~ 8.5 km long and proximal to the surface lakes on the ice
423 shelf's eastern margin (Fig. 5C). Overall, there are fewer isolated lakes towards the
424 grounding line, and the majority of the surface meltwater is proximal to the two large linear
425 systems, at elevations of ~ 60 m to 65 m (Fig. 4). The total volume and area of all surface
426 meltwater bodies is 4.9×10^7 m³ and 5.4×10^7 m² respectively (Table 1). The mean water
427 depth of all identified water bodies is 0.9 m and the maximum water depth is 4.7 m (Table
428 1).

429
430 By 26th January 2017 (Fig. 5D), the total volume and area of surface meltwater reaches a
431 peak for the summer, at 5.5×10^7 m³ and 9.1×10^7 m² respectively (Table 1). This is
432 facilitated by the enlargement of the two large linear systems, which involves the flooding of
433 topographic lows as water appears towards the firm further north on the ice shelf. These
434 linear systems are now (a) ~ 20.5 km and (b) ~ 16.9 km in length, and have a mean depth
435 of (a) 0.8 m and (b) 0.7 m. The mean depth of all water on 26th January 2017 is 0.6 m and
436 the maximum water depth is 3.3 m (Table 1).

437
438 By 13th February (Fig 5E), the two large linear systems remain prominent on the ice shelf,
439 but they have lost area, depth and volume at their southern ends. The mean water depth of
440 all water is 0.6 m and the maximum water depth is 4.3 m (Table 1). The total volume and
441 area of surface meltwater bodies falls to 3.7×10^7 m³ and 6.3×10^7 m² (Table 1), reflecting
442 the shrinkage of the two linear systems.

443

444 **4.2 Tracking Results**

445

446 Of the 1598 water bodies identified and tracked within the maximum extent matrix, 1458
447 (91%) are defined as always circular, 42 (3%) are identified as always linear, 51 (3%) are
448 defined as simple transitions, and 47 (3%) are categorised as envelopment transitions.
449 Water bodies that are always circular are predominantly clustered further south on the ice
450 shelf towards the grounding line, while water bodies defined as envelopment transitions are
451 found further north, towards the ice-shelf front (Fig. 6).

452

453 **4.2.1 Total Area and Volume of Tracked Surface Water Bodies**

454

455 For each of the tracked water body categories, Table 2 shows the maximum area and
456 volume, and the corresponding dates on which these maxima were reached. The minimum
457 area and volume for all tracked categories is zero on 14th November 2016, as no deep
458 surface melt water was detected on that date. Although 91% of water bodies identified are
459 classified as circular, they do not dominate the total area or volume of surface meltwater
460 (Table 2, Fig. 7). Conversely, the envelopment transitions, of which there are only 47 in total,
461 peak at $8.0 \times 10^7 \text{ m}^2$ in area and $4.5 \times 10^7 \text{ m}^3$ in volume on 26th January 2017, over a month
462 later than the peaks in area and volume recorded for the other three categories. These
463 envelopment transitions dominate the total area and volume signals for ‘all water bodies’
464 (Table 2), which also reach their maxima on 26th January (Table 2, Fig. 7). Between 17th
465 December 2016 and 27th December 2016 ‘all water bodies’ are characterised by
466 ‘deepening’, as their total volume increases at a greater rate than their total area, and their
467 mean depth increases (Tables 1 and 2, Fig. 7). Whereas between the 27th December and
468 the 26th January, ‘all water bodies’ are characterised by ‘spreading’, as their total area
469 increases at a faster rate than their total volume, and the mean water body depth decreases
470 (Tables 1 and 2, Fig. 7).

471

472 **4.2.2 Tracking Individual Water Bodies**

473

474 In addition to quantifying total surface water area and volume for each of the four water body
475 categories (Fig. 7, Table 2), the FASTISh algorithm also tracks changes in the area and
476 volume of *individual* water bodies. Over the 2016-2017 melt season, the two largest
477 envelopment transitions, referred to as the Western System (WS) and the Eastern System
478 (ES) hereafter, propagate towards the ice-shelf front as the melt season progresses, and
479 contain 62.6 % of the total surface water volume on 26th January 2017. The remainder of
480 this sub-section focuses solely on presenting the tracking results for these two water bodies.

481

482 The WS is active between 11th December 2016 to 25th February 2017. The area and volume
483 of meltwater within the WS reaches a maximum of $4.6 \times 10^7 \text{ m}^2$ and $2.5 \times 10^7 \text{ m}^3$ respectively
484 on 26th January 2017 (Fig. 8). The ES has a shorter lifespan, and is active between 27th
485 December 2016 and 25th February 2017 (Fig. 8). The area and volume of the ES peaks at
486 $1.9 \times 10^7 \text{ m}^2$ and $9.6 \times 10^6 \text{ m}^3$ on the 26th January 2017. Figure 9 shows the surface
487 elevation profiles for the WS and the ES, which are extracted from the maximum extent

488 mask (see section 3.5). Both systems are characterised by a surface sloping downwards
489 towards the ice-shelf front. The WS has a very shallow slope, with the elevation decreasing
490 by ~ 2 m over the 25.7 km profile (Fig. 9a); the ES is slightly steeper, showing a ~ 6 m
491 decrease in elevation over its 27 km profile (Fig. 9b).

492

493 **4.2.3 Identifying Individual Lake Freeze Through/Drainage Events.**

494

495 Previous studies have attempted to identify rapid drainage events, defined as events where
496 lakes lose > 80 % of their maximum volume in \leq four days (e.g. Fitzpatrick et al., 2014; Miles
497 et al., 2017; Williamson et al., 2018b). Here, however, the temporal resolution of available
498 imagery for the Nivlisen Ice Shelf is not high enough to allow this. Therefore, we used the
499 calculated volume time series to identify water bodies in the ‘always circular’ category that
500 lost > 80 % of their maximum volume over the full melt season, through either drainage or
501 freeze through. We focus solely on the ‘always circular’ category to better understand the
502 local loss of surface melt water in seemingly isolated and stationary water bodies. These
503 events are referred to as ‘loss events’ hereafter.

504

505 Figure 10 shows the loss in water volume through freeze-through or drainage for the ‘always
506 circular’ category over the melt season, together with the seven day moving average for the
507 mean daily and daily maximum near-surface air temperatures over the ice shelf from the
508 MetUM simulation. This shows that 805 lakes have a ‘loss event’ by 18th December 2017,
509 losing a total volume of 1.5×10^7 m³, which occurs following sustained relatively warmer
510 atmospheric conditions since the beginning of December 2016, e.g. characterised by daily
511 maximum near-surface air temperatures reaching 0°C.

512

513 **5 Discussion**

514

515 **5.1 Spatial and Temporal Distribution of Surface Meltwater Bodies**

516

517 In the early melt season, surface meltwater on the Nivlisen Ice Shelf ponds in small surface
518 lakes that form in relatively flat areas towards the grounding line, in close proximity to
519 Shirmacheroasen and the blue ice regions (Figs. 4 and 5). This initial generation of surface
520 meltwater is likely driven by regional wind patterns and the effects of local ice-albedo, as the
521 relatively low albedo of the blue ice can lead to increased local melt rates (Lenaerts et al.,
522 2017; Bell et al., 2018; Stokes et al., 2019). Furthermore, areas of lower elevation towards
523 the grounding line are likely to be exposed to katabatic winds, which can result in near-
524 surface temperatures that are 3 K greater than temperatures further up-ice and down-ice
525 (Lenaerts et al. 2017). These persistent katabatic winds can also result in the production of
526 blue ice regions, as snow is eroded from the ice-shelf surface (Lenaerts et al., 2017). Our
527 results for the early melt season on the Nivlisen Ice Shelf therefore support the findings of
528 Kingslake et al. (2017) who found, for a variety of ice shelves around Antarctica, that 50 %
529 of the ice-shelf drainage systems are either within 8 km of rock exposures, or within 3.6 km
530 of blue ice surfaces.

531

532 Seasonal variations in the amount of surface meltwater on the Nivlisen Ice Shelf are driven
533 by temperature fluctuations, with increases in surface water area and volume corresponding
534 with rising mean daily near-surface temperatures and daily maximum near-surface
535 temperatures (Fig. 10). However, as the melt season progresses, there is a transition to a
536 connected surface drainage network, which facilitates a progressive transfer of surface
537 meltwater away from the grounding line towards the ice-shelf front. As mean daily and daily
538 maximum temperatures rise and surface water bodies increase in area and volume (Fig.10),
539 they grow, merge with nearby water bodies, and form new extended networks of surface
540 water on the ice-shelf surface. While rising near-surface temperatures are a strong control
541 on the amount of surface meltwater, the direction and extent of the identified lateral water
542 transfer is controlled by the ice shelf's surface topography (Fig. 4b). Over the course of the
543 melt season, the area and volume of surface meltwater decreases in the regions close to
544 the grounding line, and increases in more distal parts of the ice shelf.
545

546 The development of the two largest enveloping water bodies (WS and ES) dominate the
547 transition to a generally more connected drainage network. This is because these systems
548 facilitate large-scale transfer of water across the shelf, as water ponds within linear
549 depressions. The ES and WS appear to be fed by smaller circular and linear surface
550 meltwater bodies, and as the area and volume of the ES and WS increases, they spread
551 and envelope nearby water bodies. Smaller water bodies likely contribute surface melt to
552 the ES and WS by (i) overtopping their local basin sides and flowing over impermeable ice,
553 which may be refrozen surface or shallow subsurface meltwater from previous years
554 (Kingslake et al., 2015) or (ii) percolating into the firn pack and spreading laterally towards
555 the ES and WS. However, the 'pulse' forward of the ES and WS between 27th December
556 2016 and 26th January 2017 does not appear to be controlled by a topographic 'lip' or
557 'dam'. It is therefore likely to primarily be the result of increased meltwater production,
558 resulting in saturation of the surrounding firn pack, which may bring it up to isothermal
559 conditions, thereby facilitating further melt and lateral transfer.
560

561 By 26th January 2017, the ES and WS are the dominant features within the entire Nivlisen
562 Ice Shelf meltwater system, together holding 62.6% of the surface meltwater volume. On
563 this date, the ES and WS reach a length of ~ 16.9 km and ~ 20.5 km respectively,
564 although unlike observations on the Nansen Ice Shelf (Bell et al., 2017), they do not
565 facilitate the export of surface meltwater off the ice-shelf front via a waterfall. Instead, both
566 systems always terminate at least ~ 35 – 55 km from the ice-shelf front, suggesting that
567 the water percolates into the surrounding firn in that area of the ice shelf. This interpretation
568 is supported by Figure 11 which shows a Sentinel-1 SAR image (Fig 11b), from 26th
569 January 2017 together with the Sentinel-2 image (Fig 11a). Areas of low backscatter
570 (appearing as dark areas in the image) are widespread across the tributary glaciers and
571 extend across the grounding line onto the upper part of the ice shelf. Whilst areas of low
572 backscatter may result from snow-grain size, surface topography/roughness, and internal
573 stratigraphy (Rott and Mätzler, 1987), it seems more likely that areas of low backscatter
574 north of the blue ice areas represent saturated firn and/or surface melt (Bindschadler and
575 Vornberger, 1992; Miles et al., 2017). Areas of low backscatter clearly extend beyond
576 areas of visible surface melt in the optical imagery, indicating the presence of subsurface

577 meltwater. For example, there are prominent areas of low backscatter (~ -5 to -15 dB)
578 extending ~ 10 km north of both the ES and WS as detected by FASTISh (Fig 11b). This
579 shows that the linear water features visible in the optical imagery are part of much larger
580 water bodies, with a lot of the water existing as slush at the surface or in the shallow
581 subsurface.

582

583 Whilst the drainage system currently observed on the Nivlisen Ice Shelf does not transfer
584 surface meltwater all the way to the ice-shelf front, it is plausible that such a system could
585 develop in the future as the quantity of surface meltwater produced increases. Whilst the
586 water may pond, (possibly resulting in eventual hydrofracture and ice-shelf collapse), the
587 ES and WS may also evolve quickly and efficiently, over increasingly saturated firn layers,
588 to allow water to flow off the ice-shelf front, thereby exporting some excess meltwater and
589 mitigating the potential threat to the ice shelf (Bell et al., 2017; Banwell, 2017).

590

591 Overall, 1.6 % of the Nivlisen Ice Shelf is occupied by some form of surface meltwater body
592 at some point during the 2016-2017 melt season, and over those areas, the mean water
593 depth is 0.85 m. Comparatively, prior to its collapse, 5.3 % the Larsen B Ice Shelf was
594 covered by a surface meltwater body, and the mean water depth was 0.82 m (Banwell et
595 al., 2014). Whilst the mean water body depths between the Larsen B and Nivlisen Ice
596 Shelves are comparable, the spatial distributions of these water bodies, and the proportion
597 of the ice shelf that they cover, are different. Surface water bodies were distributed relatively
598 evenly across the entire surface of Larsen B before it collapsed, whereas surface water
599 bodies are predominantly clustered towards the grounding line on the Nivlisen Ice Shelf, and
600 the transfer of surface melt towards the ice-shelf front and across snow/ firn-covered regions
601 is predominantly facilitated by the larger WS and ES. The development of these large, linear
602 water bodies is likely facilitated by topography, and allows the transfer of summer meltwater
603 towards the ice-shelf front. This large scale lateral transfer of meltwater is further facilitated
604 as the ES and WS develop over frozen meltwater paths from previous years (Kingslake et
605 al., 2015).

606

607 **5.2 Loss of Water Volume from Circular Surface Water Bodies**

608

609 The loss of 1.5×10^7 m³ of surface water from the circular water bodies by 27th December
610 2017 follows sustained relatively warmer atmospheric conditions since the beginning of
611 December 2017 (Fig. 10), and coincides with an increase in the total surface water volume
612 on the ice shelf (Fig 10b). In particular, we see an increase in the volume of water held within
613 the enveloping water bodies, which continues to increase up to a maximum of 4.5×10^7 m³
614 on 26th January 2017 (Fig. 7). It is likely, therefore, that the loss of water from circular water
615 bodies at this early stage in the melt season signifies the lateral transfer of water away from
616 the small 'isolated' bodies near the grounding line into the large enveloping water bodies
617 which hold and transport the surface meltwater across the ice shelf to more distal regions.
618 This lateral transfer of water may be occurring through two mechanisms: (i) the over-topping
619 of surface lakes, which results in the formation of shallow channels that connect water
620 bodies and facilitate the transfer of water towards the ice-shelf front (e.g. Banwell et al.,

621 2019), or (ii) the gradual percolation of surface meltwater into the cold firn pack, which
622 reduces the firn air content (FAC) of a region (Lenaerts et al., 2017), therefore creating an
623 impermeable surface over which water can flow (e.g. Kingslake et al., 2015). The firn may
624 also become saturated enough to be isothermal, therefore melting and facilitating the flow
625 of upstream ponded meltwater. This is particularly likely to occur near surface depressions
626 such as those that are later occupied by the WS and ES.

627

628 **5.3 Potential Implications for Ice-Shelf Stability**

629 It is expected that the area of coverage and volume of surface meltwater on Antarctic ice
630 shelves will increase into the future, in line with rising atmospheric temperatures (Bell et
631 al., 2018; IPCC, 2019; Kingslake et al., 2017; Siegert et al., 2019). This surface water may
632 have significant implications for ice-shelf stability, as meltwater accumulation can lead to
633 hydrofracture which could subsequently result in the collapse of an ice shelf, as seen on
634 the Larsen B Ice Shelf in 2002 (Robel and Banwell, 2019; Banwell et al., 2013). An ice
635 shelf may become increasingly vulnerable to hydrofracture if its FAC is reduced (Lenaerts
636 et al., 2017). On ice shelves like Nivlisen, where large-scale lateral water transfer prevails,
637 meltwater is delivered to locations that may otherwise not receive or experience much melt
638 (Bell et al., 2017), and the FAC of these locations will, in turn, be reduced, increasing their
639 susceptibility to surface meltwater ponding and hydrofracture.

640 Surface meltwater re-freezing at the end of the melt season will also act as a significant
641 source of heat, and the lateral transfer of surface melt could cause increased warming of
642 the ice shelf and possible weakening in areas which currently do not experience significant
643 summer melt. Were the maximum volume of surface meltwater we observe on the Nivlisen
644 Ice Shelf in the 2016-2017 melt season ($5.5 \times 10^7 \text{ m}^3$) to re-freeze over the maximum area
645 of surface meltwater ($9.1 \times 10^7 \text{ m}^2$), it would release an amount of energy equivalent to 49
646 days of potential solar energy receipts (calculated using the methods of Arnold and Rees
647 (2009)), assuming an ice surface albedo of 0.86; the mean value calculated for a water-
648 free distal area of the ice shelf. Furthermore, large-scale lateral water transfer and
649 subsequent ponding may lead to ice-shelf flexure (and therefore potential fracture) at
650 locations that may have otherwise not been affected by flexure in response to meltwater
651 loading (Banwell et al., 2013, 2019; Macayeal and Sergienko, 2013). However, evidence
652 of lateral water transfer and export off the Nansen Ice Shelf has highlighted the potential
653 for surface drainage systems to mitigate some of these meltwater driven instabilities (Bell
654 et al., 2017).

655

656 **6 Conclusions**

657

658 We have adapted the pre-existing FASTER algorithm, developed for studying lakes on the
659 GrIS (Williamson et al., 2018b), so that we can identify and track the area, depth and volume
660 of water bodies across Antarctic ice shelves. We refer to this new algorithm as FASTISh,
661 and have used it to study the changing geometry and spatial patterns of water bodies across

662 the Nivlisen Ice Shelf in the 2016-2017 melt season. In total, we identify and track 1598
663 water bodies on the ice shelf over the course of the melt season. Surface water is initially
664 generated towards the nunatak and blue ice region, in proximity to the grounding line. This
665 region is relatively flat and has a low albedo, and we therefore observe localised ponding of
666 surface meltwater. As the melt season progresses and mean daily and daily maximum
667 temperatures increase, we see a transition from isolated, localised ponding towards the
668 grounding line to a more connected drainage system that is influenced by the ice-shelf
669 topography. The middle of the melt season (e.g. 27th December 2016) is characterised by
670 the progression of surface melt water bodies towards the ice-shelf front, as two large
671 extensive drainage systems (the East System (ES) and West System (WS)) develop in long
672 linear surface depressions. [Around the peak of the melt season \(26th January 2017\)](#), the ES
673 and WS have developed to their largest observed extent, and facilitate the lateral transfer
674 of surface melt up to 16.9 and 20.5 km north, into the firn pack and towards the ice-shelf
675 front. The transfer of surface meltwater to regions on the ice shelf that otherwise experience
676 little surface melt may have implications for the structure and stability of the ice shelf in the
677 future. Our findings could be useful in comparing to IceSat 2 derived lake depths, in addition
678 to constraining future ice-shelf surface hydrology models.

679

680

681 **Code and Data Availability**

682 The satellite imagery, REMA data, and meteorological data are all open access (see section
683 3). The MATLAB scripts used to process the data will be freely available from Apollo
684 Repository (<https://www.repository.cam.ac.uk/>) upon publication.

685

686 **Author Contributions**

687 RLD developed the methodology and scripts, building on the prior work of AGW. NSA
688 developed the script to convert Landsat DN values to per-pixel TOA values. AO performed
689 the Regional Climate Model run using the Met Office Unified Model to provide the
690 meteorological data. RLD conducted all other analysis and wrote the draft manuscript, under
691 the supervision of all other authors. All authors discussed the results and were involved in
692 editing of the manuscript.

693

694

695 **Competing Interests**

696 The authors declare no competing interests

697

698

699 **Acknowledgements**

700

701 We sincerely thank Mahsa Moussavi and Allen Pope for their guidance and many productive
702 discussions over the past two years. Rebecca Dell acknowledges support from a Natural
703 Environment Research Council Doctoral Training Partnership Studentship (Grant number:
704 NE/L002507/1; CASE Studentship with the British Antarctic Survey). Ian Willis
705 acknowledges support from NERC Grant G102130. This paper was written while Ian Willis
706 was in receipt of a Cooperative Institute for Research in Environmental Science (CIRES)

707 Visiting Sabbatical Fellowship and he thanks in particular Waleed Abdalati, Ted Scambos,
708 Kristy Tiampo and Mike Willis for their hospitality. Alison Banwell acknowledges support
709 from a CIRES Visiting Postdoctoral Fellowship and a grant from the US National Science
710 Foundation (#1841607) awarded to the University of Colorado, Boulder. AO thanks Tony
711 Phillips (BAS) for converting the MetUM output to daily averaged fields. DEMs provided by
712 the Byrd Polar and Climate Research Center and the Polar Geospatial Center under
713 NSF-OPP awards 1543501, 1810976, 1542736, 1559691, 1043681, 1541332,
714 0753663, 1548562, 1238993 and NASA award NNX10AN61G. Computer time
715 provided through a Blue Waters Innovation Initiative. DEMs produced using data from
716 DigitalGlobe, Inc.

717

718

719 **References**

720

- 721 Arnold, N. and Rees, G.: Effects of digital elevation model spatial resolution on distributed
722 calculations of solar radiation loading on a high arctic glacier, *J. Glaciol.*, 55(194), 973–
723 984, doi:10.3189/002214309790794959, 2009.
- 724 Arnold, N. S., Banwell, A. F. and Willis, I. C.: High-resolution modelling of the seasonal
725 evolution of surface water storage on the Greenland Ice Sheet, *Cryosph.*, 8(4), 1149–
726 1160, doi:10.5194/tc-8-1149-2014, 2014.
- 727 Banwell, A.: Glaciology: Ice-shelf stability questioned, *Nature*, 544(7650), 306–307,
728 doi:10.1038/544306a, 2017.
- 729 Banwell, A. F. and MacAyeal, D. R.: Ice-shelf fracture due to viscoelastic flexure stress
730 induced by fill/drain cycles of supraglacial lakes, *Antarct. Sci.*, 27(6), 587–597,
731 doi:10.1017/S0954102015000292, 2015.
- 732 Banwell, A. F., MacAyeal, D. R. and Sergienko, O. V.: Breakup of the Larsen B Ice Shelf
733 triggered by chain reaction drainage of supraglacial lakes, *Geophys. Res. Lett.*, 40(22),
734 5872–5876, doi:10.1002/2013GL057694, 2013.
- 735 Banwell, A. F., Caballero, M., Arnold, N. S., Glasser, N. F., Cathles, L. Mac and MacAyeal,
736 D. R.: Supraglacial lakes on the Larsen B ice shelf, Antarctica, and at Paakitsoq, West
737 Greenland: A comparative study, *Ann. Glaciol.*, 55(66), 1–8,
738 doi:10.3189/2014AoG66A049, 2014.
- 739 Banwell, A. F., Willis, I. C., Macdonald, G. J., Goodsell, B. and MacAyeal, D. R.: Direct
740 measurements of ice-shelf flexure caused by surface meltwater ponding and drainage,
741 *Nat. Commun.*, 10(1), 1–10, doi:10.1038/s41467-019-08522-5, 2019.
- 742 Bell, R. E., Chu, W., Kingslake, J., Das, I., Tedesco, M., Tinto, K. J., Zappa, C. J.,
743 Frezzotti, M., Boghosian, A. and Lee, W. S.: Antarctic ice shelf potentially stabilized by
744 export of meltwater in surface river, *Nature*, 544(7650), 344–348,
745 doi:10.1038/nature22048, 2017.
- 746 Bell, R. E., Banwell, A. F., Trusel, L. D. and Kingslake, J.: Antarctic surface hydrology and
747 impacts on ice-sheet mass balance, *Nat. Clim. Chang.*, 8(12), 1044–1052,
748 doi:10.1038/s41558-018-0326-3, 2018.
- 749 Bevan, S. L., Luckman, A., Hubbard, B., Kulesa, B., Ashmore, D., Kuipers Munneke, P.,
750 O’Leary, M., Booth, A., Sevestre, H. and McGrath, D.: Centuries of intense surface melt on
751 Larsen C Ice Shelf, *Cryosphere*, 11(6), 2743–2753, doi:10.5194/tc-11-2743-2017, 2017.
- 752 Bindshadler, R. and Vornberger, P.: Interpretation of SAR imagery of the Greenland ice
753 sheet using coregistered TM imagery, *Remote Sens. Environ.*, 42(3), 167–175 [online]
754 Available from: <https://www.sciencedirect.com/science/article/pii/003442579290100X>
755 (Accessed 15 May 2018), 1992.

756 Bush, M., Allen, T., Bain, C., Boutle, I., Edwards, J., Finnenkoetter, A., Franklin, C.,
757 Hanley, K., Lean, H., Lock, A., Manners, J., Mittermaier, M., Morcrette, C., North, R.,
758 Petch, J., Short, C., Vosper, S., Walters, D., Webster, S., Weeks, M., Wilkinson, J., Wood,
759 N. and Zerroukat, M.: The first Met Office Unified Model/JULES Regional Atmosphere and
760 Land configuration, RAL1, Geosci. Model Dev. Discuss., 1–47, doi:10.5194/gmd-2019-
761 130, 2019.

762 Cook, A. J. and Vaughan, D. G.: Overviewing of areal changes of the ice shelves on the
763 Antarctic Peninsula over the past 50 years, *Cryosph.*, 4, 77–98 [online] Available from:
764 <http://dro.dur.ac.uk/20037/1/20037.pdf> (Accessed 7 June 2018), 2010.

765 Datta, R. T., Tedesco, M., Fettweis, X., Agosta, C., Lhermitte, S., Lenaerts, J. T. M. and
766 Wever, N.: The Effect of Foehn-Induced Surface Melt on Firn Evolution Over the Northeast
767 Antarctic Peninsula, *Geophys. Res. Lett.*, 46(7), 3822–3831, doi:10.1029/2018GL080845,
768 2019.

769 DeConto, R. M. and Pollard, D.: Contribution of Antarctica to past and future sea-level rise,
770 *Nature*, 531(7596), 591–597, doi:10.1038/nature17145, 2016.

771 Dee, D. P., Uppala, S. M., Simmons, A. J., Berrisford, P., Poli, P., Kobayashi, S., Andrae,
772 U., Balmaseda, M. A., Balsamo, G., Bauer, P., Bechtold, P., Beljaars, A. C. M., van de
773 Berg, L., Bidlot, J., Bormann, N., Delsol, C., Dragani, R., Fuentes, M., Geer, A. J.,
774 Haimberger, L., Healy, S. B., Hersbach, H., Hólm, E. V., Isaksen, I., Kållberg, P., Köhler,
775 M., Matricardi, M., McNally, A. P., Monge-Sanz, B. M., Morcrette, J. J., Park, B. K.,
776 Peubey, C., de Rosnay, P., Tavolato, C., Thépaut, J. N. and Vitart, F.: The ERA-Interim
777 reanalysis: Configuration and performance of the data assimilation system, *Q. J. R.*
778 *Meteorol. Soc.*, 137(656), 553–597, doi:10.1002/qj.828, 2011.

779 Dow, C. F., Lee, W. S., Greenbaum, J. S., Greene, C. A., Blankenship, D. D., Poinar, K.,
780 Forrest, A. L., Young, D. A. and Zappa, C. J.: Basal channels drive active surface
781 hydrology and transverse ice shelf fracture, *Sci. Adv.*, 4(6), eaao7212,
782 doi:10.1126/sciadv.aao7212, 2018.

783 Echelmeyer, K., Clarke, T. S. and Harrison, W. D.: Surficial glaciology of Jakobshavns
784 Isbrae, West Greenland: part I. Surface morphology, *J. Glaciol.*, 37(127), 368–382,
785 doi:10.1017/S0022143000005803, 1991.

786 Fitzpatrick, A. A. W., Hubbard, A. L., Box, J. E., Quincey, D. J., Van As, D., Mikkelsen, A.
787 P. B., Doyle, S. H., Dow, C. F., Hasholt, B. and Jones, G. A.: A decade (2002-2012) of
788 supraglacial lake volume estimates across Russell Glacier, West Greenland, *Cryosphere*,
789 8(1), 107–121, doi:10.5194/tc-8-107-2014, 2014.

790 Fürst, J. J., Durand, G., Gillet-Chaulet, F., Tavard, L., Rankl, M., Braun, M. and
791 Gagliardini, O.: The safety band of Antarctic ice shelves, *Nat. Clim. Chang.*, 6(5), 479–482,
792 doi:10.1038/nclimate2912, 2016.

793 Glasser, N. F. and Gudmundsson, G. H.: Longitudinal surface structures (flowstripes) on
794 Antarctic glaciers, *Cryosphere*, 6(2), 383–391, doi:10.5194/tc-6-383-2012, 2012.

795 Glasser, N. F. and Scambos, T. A.: A structural glaciological analysis of the 2002 Larsen B
796 ice-shelf collapse, *J. Glaciol.*, 54(184), 3–16, doi:10.3189/002214308784409017, 2008.

797 Gudmundsson, G. H., Paolo, F. S., Adusumilli, S. and Fricker, H. A.: Instantaneous
798 Antarctic ice-sheet mass loss driven by thinning ice shelves, *Geophys. Res. Lett.*,
799 2019GL085027, doi:10.1029/2019GL085027, 2019.

800 Hall, D. K., Branch, H. S., Tait, A. B., Riggs, G. A., Corporation, D. S., Salomonson, V. V.,
801 Directorate, E. S., Chien, J. Y. L., Corporation, G. S. and Klein, A. G.: Algorithm
802 Theoretical Basis Document (ATBD) for the MODIS Snow-, Lake Ice- and Sea Ice-
803 Mapping Algorithms, Analysis [online] Available from:
804 https://eosps.nasa.gov/sites/default/files/atbd/atbd_mod10.pdf (Accessed 21 April
805 2019), 2001.

806 Horwath, M., Dietrich, R., Baessler, M., Nixdorf, U., Steinhage, D., Fritzsche, D., Damm, V.
807 and Reitmayr, G.: Nivlisen, an Antarctic ice shelf in Dronning Maud Land: Geodetic-
808 glaciological results from a combined analysis of ice thickness, ice surface height and ice-
809 flow observations, *J. Glaciol.*, 52(176), 17–30, doi:10.3189/172756506781828953, 2006.

810 Howat, I. M., Porter, C., Smith, B. E., Noh, M. J. and Morin, P.: The reference elevation
811 model of antarctica, *Cryosphere*, 13(2), 665–674, doi:10.5194/tc-13-665-2019, 2019.

812 Hubbard, B., Luckman, A., Ashmore, D. W., Bevan, S., Kulesa, B., Kuipers Munneke, P.,
813 Philippe, M., Jansen, D., Booth, A., Sevestre, H., Tison, J. L., O’Leary, M. and Rutt, I.:
814 Massive subsurface ice formed by refreezing of ice-shelf melt ponds, *Nat. Commun.*, 7,
815 doi:10.1038/ncomms11897, 2016.

816 Hui, F., Ci, T., Cheng, X., Scambos, T. A., Liu, Y., Zhang, Y., Chi, Z., Huang, H., Wang, X.,
817 Wang, F., Zhao, C., Jin, Z. and Wang, K.: Mapping blue-ice areas in Antarctica using
818 ETM+ and MODIS data, *Ann. Glaciol.*, 55(66), 129–137, doi:10.3189/2014AoG66A069,
819 2014.

820 IPCC: Special Report on the Ocean and Cryosphere in a Changing Climate - Technical
821 Summary (Final Draft). [online] Available from: <https://www.ipcc.ch/srocc/> (Accessed 18
822 December 2019), 2019.

823 Kingslake, J., Ng, F. and Sole, A.: Modelling channelized surface drainage of supraglacial
824 lakes, *J. Glaciol.*, 61(225), 185–199, doi:10.3189/2015JoG14J158, 2015.

825 Kingslake, J., Ely, J. C., Das, I. and Bell, R. E.: Widespread movement of meltwater onto
826 and across Antarctic ice shelves, *Nature*, 544(7650), 349–352, doi:10.1038/nature22049,
827 2017.

828 Koziol, C., Arnold, N., Pope, A. and Colgan, W.: Quantifying supraglacial meltwater
829 pathways in the Paakitsoq region, West Greenland, *J. Glaciol.*, 63(239), 464–476,
830 doi:10.1017/jog.2017.5, 2017.

831 Kuipers Munneke, P., Ligtenberg, S. R. M., Van Den Broeke, M. R. and Vaughan, D. G.:
832 Firn air depletion as a precursor of Antarctic ice-shelf collapse, *J. Glaciol.*, 60(220), 205–
833 214, doi:10.3189/2014JoG13J183, 2014.

834 Langley, E. S., Leeson, A. A., Stokes, C. R. and Jamieson, S. S. R.: Seasonal evolution of
835 supraglacial lakes on an East Antarctic outlet glacier, *Geophys. Res. Lett.*, 43(16), 8563–
836 8571, doi:10.1002/2016GL069511, 2016.

837 Leeson, A. A., Forster, E., Rice, A., Gourmelen, N. and van Wessem, J. M.: Evolution of
838 Supraglacial Lakes on the Larsen B Ice Shelf in the Decades Before it Collapsed,
839 *Geophys. Res. Lett.*, 47(4), doi:10.1029/2019GL085591, 2020.

840 Lenaerts, J., Lhermitte, S., Drews, R., Ligtenberg, S. R. M., Berger, S., Helm, V., Smeets,
841 P. C. J. P., van den Broeke, M. R., van De Berg, W. J., van Meijgaard, E., Eijkelboom, M.,
842 Eisen, O. and Pattyn, F.: Meltwater produced by wind – albedo interaction stored in an
843 East Antarctic ice shelf, *Nat. Clim. Chang.*, 7, 58–63, doi:10.1038/NCLIMATE3180, 2017.

844 Liston, G. E. and Winther, J. G.: Antarctic surface and subsurface snow and ice melt
845 fluxes, *J. Clim.*, 18(10), 1469–1481, doi:10.1175/JCLI3344.1, 2005.

846 Liston, G. E., Winther, J. G., Bruland, O., Elvehøy, H. and Sand, K.: Below-surface ice
847 melt on the coastal Antarctic ice sheet, *J. Glaciol.*, 45(150), 273–285,
848 doi:10.3189/s0022143000001775, 1999.

849 Luckman, A., Elvidge, A., Jansen, D., Kulesa, B., Kuipers Munneke, P., King, J. and
850 Barrand, N. E.: Surface melt and ponding on Larsen C Ice Shelf and the impact of föhn
851 winds, *Antarct. Sci.*, 26(6), 625–635, doi:10.1017/S0954102014000339, 2014.

852 Macayeal, D. R. and Sergienko, O. V.: The flexural dynamics of melting ice shelves, *Ann.*
853 *Glaciol.*, 54(63), 1–10, doi:10.3189/2013AoG63A256, 2013.

854 Macdonald, G. J., Banwell, A. F. and Macayeal, D. R.: Seasonal evolution of supraglacial
855 lakes on a floating ice tongue , Petermann Glacier , Greenland, , 1–10,

856 doi:10.1017/aog.2018.9, 2018.

857 McGrath, D., Steffen, K., Rajaram, H., Scambos, T., Abdalati, W. and Rignot, E.: Basal
858 crevasses on the Larsen C Ice Shelf, Antarctica: Implications for meltwater ponding and
859 hydrofracture, *Geophys. Res. Lett.*, 39(16), n/a-n/a, doi:10.1029/2012GL052413, 2012.

860 Miles, K. E., Willis, I. C., Benedek, C. L., Williamson, A. G. and Tedesco, M.: Toward
861 Monitoring Surface and Subsurface Lakes on the Greenland Ice Sheet Using Sentinel-1
862 SAR and Landsat-8 OLI Imagery, *Front. Earth Sci.*, 5, doi:10.3389/feart.2017.00058, 2017.

863 Mottram, R., Hansen, N., Kittel, C., Wessem, M. van, Agosta, C., Amory, C., Boberg, F.,
864 Berg, W. J. van de, Fettweis, X., Gossart, A., Meijgaard, E. van, Orr, A., Phillips, T.,
865 Webster, S., Simonsen, S. and Souverijns, N.: What is the Surface Mass Balance of
866 Antarctica? An Intercomparison of Regional Climate Model Estimates, *Cryosph. Discuss.*,
867 1–42, doi:10.5194/tc-2019-333, 2020.

868 Mouginot, J., Scheuchl, B. and Rignot, E.: MEASUREs Antarctic Boundaries for IPY 2007-
869 2009 from Satellite Radar, Version 2., NASA Natl. Snow Ice Data Cent. Distrib. Act. Arch.
870 Center., doi:https://doi.org/10.5067/AXE4121732AD, 2017.

871 Moussavi, M. S., Abdalati, W., Pope, A., Scambos, T., Tedesco, M., MacFerrin, M. and
872 Grigsby, S.: Derivation and validation of supraglacial lake volumes on the Greenland Ice
873 Sheet from high-resolution satellite imagery, *Remote Sens. Environ.*, 183, 294–303,
874 doi:10.1016/j.rse.2016.05.024, 2016.

875 Philpot, W. D.: Bathymetric mapping with passive multispectral imagery, *Appl. Opt.*, 28(8),
876 1569, doi:10.1364/ao.28.001569, 1989.

877 Pope, A.: Reproducibly estimating and evaluating supraglacial lake depth with Landsat 8
878 and other multispectral sensors, *Earth Sp. Sci.*, 3(4), 176–188,
879 doi:10.1002/2015EA000125, 2016.

880 Pope, A., Scambos, T. A., Moussavi, M., Tedesco, M., Willis, M., Shean, D. and Grigsby,
881 S.: Estimating supraglacial lake depth in West Greenland using Landsat 8 and comparison
882 with other multispectral methods, *Cryosphere*, 10(1), 15–27, doi:10.5194/tc-10-15-2016,
883 2016.

884 Rignot, E., Casassa, G., Gogineni, P., Krabill, W., Rivera, A. and Thomas, R.: Accelerated
885 ice discharge from the Antarctic Peninsula following the collapse of Larsen B ice shelf,
886 *Geophys. Res. Lett.*, 31(18), L18401, doi:10.1029/2004GL020697, 2004.

887 Rignot, E., Mouginot, J., Scheuchl, B., Van Den Broeke, M., Van Wessem, M. J. and
888 Morlighem, M.: Four decades of Antarctic ice sheet mass balance from 1979–2017, *Proc.*
889 *Natl. Acad. Sci. U. S. A.*, 116(4), 1095–1103, doi:10.1073/pnas.1812883116, 2019.

890 Robel, A. A. and Banwell, A. F.: A Speed Limit on Ice Shelf Collapse Through
891 Hydrofracture, *Geophys. Res. Lett.*, 46(21), 12092–12100, doi:10.1029/2019GL084397,
892 2019.

893 Rott, H. and Mätzler, C.: Possibilities and Limits of Synthetic Aperture Radar for Snow and
894 Glacier Surveying, *Ann. Glaciol.*, 9, 195–199, doi:10.3189/s0260305500000604, 1987.

895 De Rydt, J., Gudmundsson, G. H., Rott, H. and Bamber, J. L.: Modeling the instantaneous
896 response of glaciers after the collapse of the Larsen B Ice Shelf, *Geophys. Res. Lett.*,
897 42(13), 5355–5363, doi:10.1002/2015GL064355, 2015.

898 Scambos, T., Hulbe, C. and Fahnestock, M.: Climate-induced ice shelf disintegration in the
899 Antarctic Peninsula, in *Antarctica Peninsula climate variability: a historical and paleo-*
900 *environmental perspective*, pp. 79–92., 2003.

901 Scambos, T., Fricker, H. A., Liu, C. C., Bohlander, J., Fastook, J., Sargent, A., Massom, R.
902 and Wu, A. M.: Ice shelf disintegration by plate bending and hydro-fracture—Satellite
903 observations and model results of the 2008 Wilkins ice shelf break-ups, *Earth Planet. Sci.*
904 *Lett.*, 280ID–6, 51–60, doi:10.1016/j.epsl.2008.12.027, 2009.

905 Scambos, T. A., Bohlander, J. A., Shuman, C. A. and Skvarca, P.: Glacier acceleration

906 and thinning after ice shelf collapse in the Larsen B embayment, Antarctica, *Geophys.*
907 *Res. Lett.*, 31(18), L18402, doi:10.1029/2004GL020670, 2004.

908 Selmes, N., Murray, T. and James, T. D.: Fast draining lakes on the Greenland Ice Sheet,
909 *Geophys. Res. Lett.*, 38(15), n/a-n/a, doi:10.1029/2011GL047872, 2011.

910 Selmes, N., Murray, T. and James, T. D.: Characterizing supraglacial lake drainage and
911 freezing on the Greenland Ice Sheet, *Cryosph. Discuss.*, 7(1), 475–505, doi:10.5194/tcd-7-
912 475-2013, 2013.

913 Sergienko, O. V.: Glaciological twins: Basally controlled subglacial and supraglacial lakes,
914 *J. Glaciol.*, 59(213), 3–8, doi:10.3189/2013JoG12J040, 2013.

915 Siegert, M., Atkinson, A., Banwell, A., Brandon, M., Convey, P., Davies, B., Downie, R.,
916 Edwards, T., Hubbard, B., Marshall, G., Rogelj, J., Rumble, J., Stroeve, J. and Vaughan,
917 D.: The Antarctic Peninsula under a 1.5°C global warming scenario, *Front. Environ. Sci.*,
918 7(JUN), doi:10.3389/fenvs.2019.00102, 2019.

919 Sneed, W. A. and Hamilton, G. S.: Evolution of melt pond volume on the surface of the
920 Greenland Ice Sheet, *Geophys. Res. Lett.*, 34(3), L03501, doi:10.1029/2006GL028697,
921 2007.

922 Sneed, W. A. and Hamilton, G. S.: Validation of a method for determining the depth of
923 glacial melt ponds using satellite imagery, *Ann. Glaciol.*, 52(59), 15–22,
924 doi:10.3189/172756411799096240, 2011.

925 Stokes, C. R., Sanderson, J. E., Miles, B. W. J., Jamieson, S. S. R. and Leeson, A. A.:
926 Widespread distribution of supraglacial lakes around the margin of the East Antarctic Ice
927 Sheet, *Sci. Rep.*, 9(1), doi:10.1038/s41598-019-50343-5, 2019.

928 Traganos, D., Poursanidis, D., Aggarwal, B., Chrysoulakis, N. and Reinartz, P.: Estimating
929 satellite-derived bathymetry (SDB) with the Google Earth Engine and sentinel-2, *Remote*
930 *Sens.*, 10(6), 859, doi:10.3390/rs10060859, 2018.

931 Vieli, A., Payne, A. J., Du, Z. and Shepherd, A.: Numerical modelling and data assimilation
932 of the Larsen B ice shelf, Antarctic Peninsula, *Philos. Trans. R. Soc. A Math. Phys. Eng.*
933 *Sci.*, 364(1844), 1815–1839, doi:10.1098/rsta.2006.1800, 2006.

934 Walters, D., Boutle, I., Brooks, M., Melvin, T., Stratton, R., Vosper, S., Wells, H., Williams,
935 K., Wood, N., Allen, T., Bushell, A., Copsey, D., Earnshaw, P., Edwards, J., Gross, M.,
936 Hardiman, S., Harris, C., Heming, J., Klingaman, N., Levine, R., Manners, J., Martin, G.,
937 Milton, S., Mittermaier, M., Morcrette, C., Riddick, T., Roberts, M., Sanchez, C., Selwood,
938 P., Stirling, A., Smith, C., Suri, D., Tennant, W., Luigi Vidale, P., Wilkinson, J., Willett, M.,
939 Woolnough, S. and Xavier, P.: The Met Office Unified Model Global Atmosphere 6.0/6.1
940 and JULES Global Land 6.0/6.1 configurations, *Geosci. Model Dev.*, 10(4), 1487–1520,
941 doi:10.5194/gmd-10-1487-2017, 2017.

942 Williamson, A. G., Arnold, N. S., Banwell, A. F. and Willis, I. C.: A Fully Automated
943 Supraglacial lake area and volume Tracking (“FAST”) algorithm: Development and
944 application using MODIS imagery of West Greenland, *Remote Sens. Environ.*, 196, 113–
945 133, doi:10.1016/j.rse.2017.04.032, 2017.

946 Williamson, A. G., Willis, I. C., Arnold, N. S. and Banwell, A. F.: Controls on rapid
947 supraglacial lake drainage in West Greenland: an Exploratory Data Analysis approach, *J.*
948 *Glaciol.*, 1–19, doi:10.1017/jog.2018.8, 2018a.

949 Williamson, A. G., Banwell, A. F., Willis, I. C. and Arnold, N. S.: Dual-satellite (Sentinel-2
950 and Landsat 8) remote sensing of supraglacial lakes in Greenland, *Cryosph. Discuss.*, 1–
951 27, doi:10.5194/tc-2018-56, 2018b.

952 Winther, J.-G. G., Elvehøy, H., Bøggild, C. E., Sand, K. and Liston, G.: Melting, runoff and
953 the formation of frozen lakes in a mixed snow and blue-ice field in Dronning Maud Land,
954 Antarctica, *J. Glaciol.*, 42(141), 271–278, doi:10.3189/s0022143000004135, 1996.

955 Wuite, J., Rott, H., Hetzenecker, M., Floricioiu, D., De Rydt, J., Gudmundsson, G. H.,

956 Nagler, T. and Kern, M.: Evolution of surface velocities and ice discharge of Larsen B
957 outlet glaciers from 1995 to 2013, *Cryosphere*, 9(3), 957–969, doi:10.5194/tc-9-957-2015,
958 2015.

959 Yang, K. and Smith, L. C.: Supraglacial streams on the Greenland Ice Sheet delineated
960 from combined spectral – shape information in high-resolution satellite imagery, *IEEE*
961 *Geosci. Remote Sens. Lett.*, 10(4), 801–805, doi:10.1109/LGRS.2012.2224316, 2013.

962

963

964

965

966

967

968

969

970

971

972

973

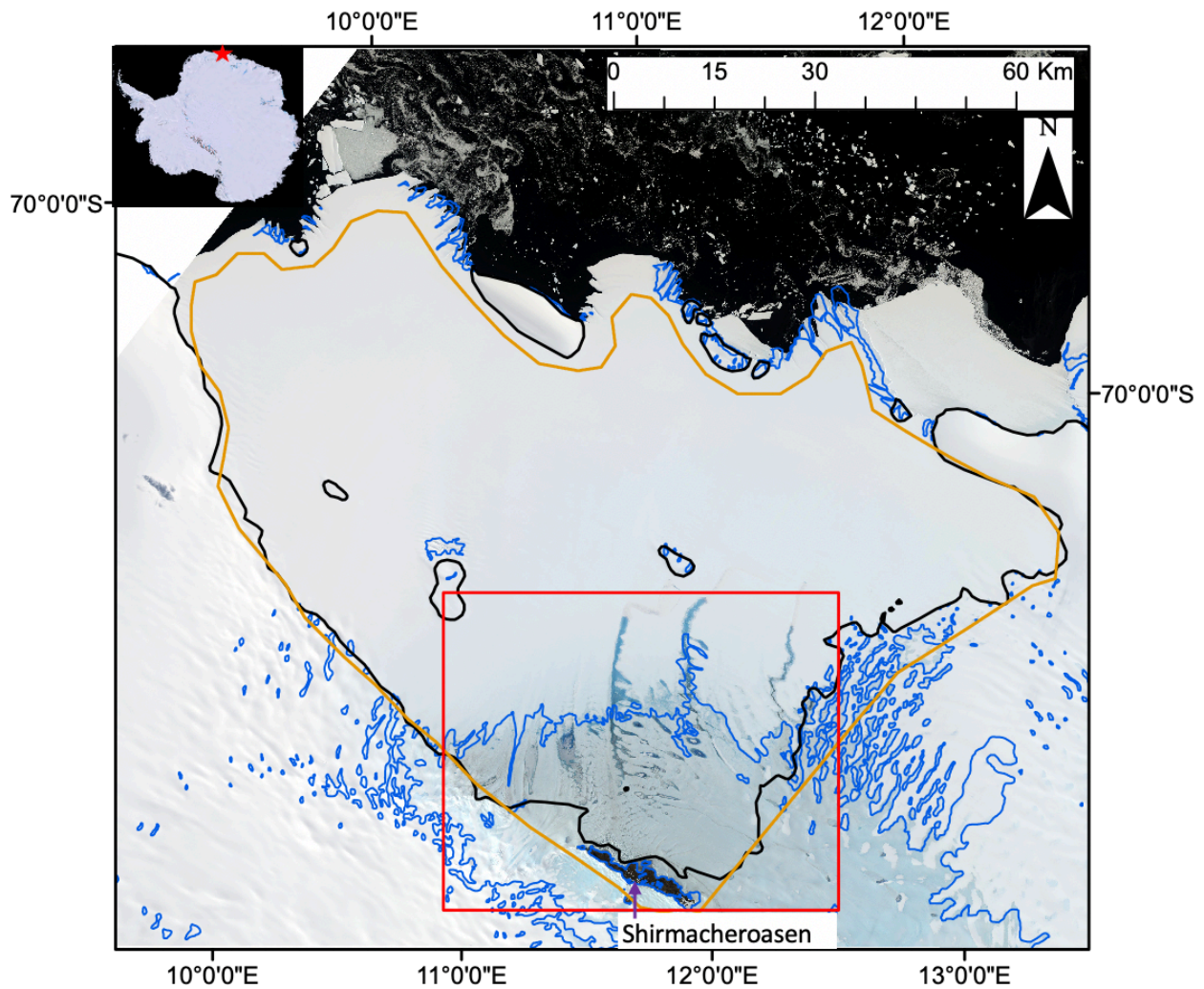
974

975

976

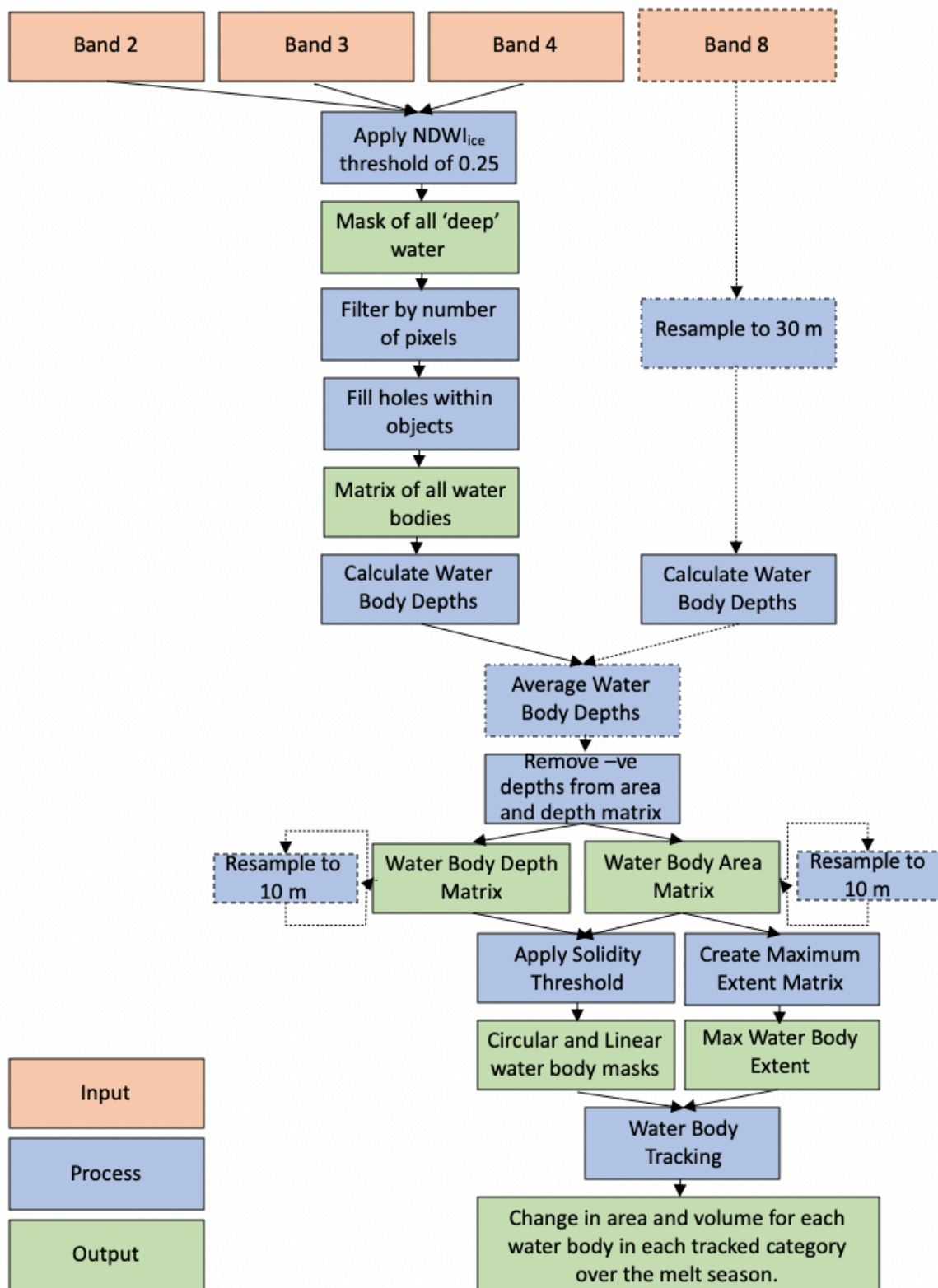
977

978



979
 980
 981
 982
 983
 984
 985
 986
 987
 988
 989
 990
 991
 992

Figure 1: A map of the study area. The base image is a mosaicked RGB Sentinel-2 image of the Nivlisen Ice Shelf acquired on 26th January 2017. The solid black line marks the grounding line, according to the NASA Making Earth System Data Records for Use in Research Environments (MEaSUREs) Antarctic boundaries dataset (Mouginot et al., 2017). The solid blue line represents the blue ice areas in the region according to Hui et al. (2014). The solid orange line shows the study area extent used for this study, and the solid red line marks the area shown in all subsequent figures. The red star on the inset shows the location of the Nivlisen Ice Shelf in the context of an image of Antarctica, which is a mosaic product based on sources from USGS, NASA, National Science Foundation, and the British Antarctic Survey (<https://visibleearth.nasa.gov/view.php?id=78592>).



993

994

995 *Figure 2: Workflow detailing the methods applied to both the Landsat 8 and Sentinel-2 images*

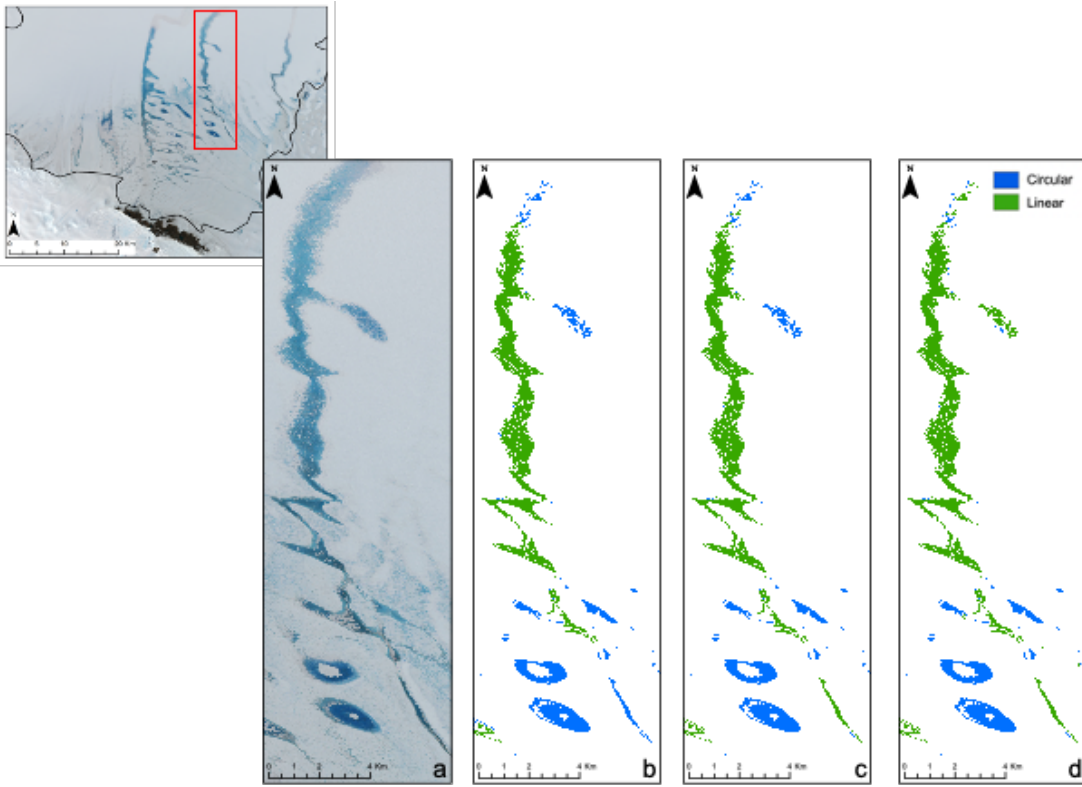
996 *through the FASTISH algorithm in MATLAB. Dashed lines indicate steps that were applied to Landsat*

997 *8 images only, whereas solid lines indicate steps that were applied to both sets of image types.*

998 *Modified from Williamson et al. (2018b).*

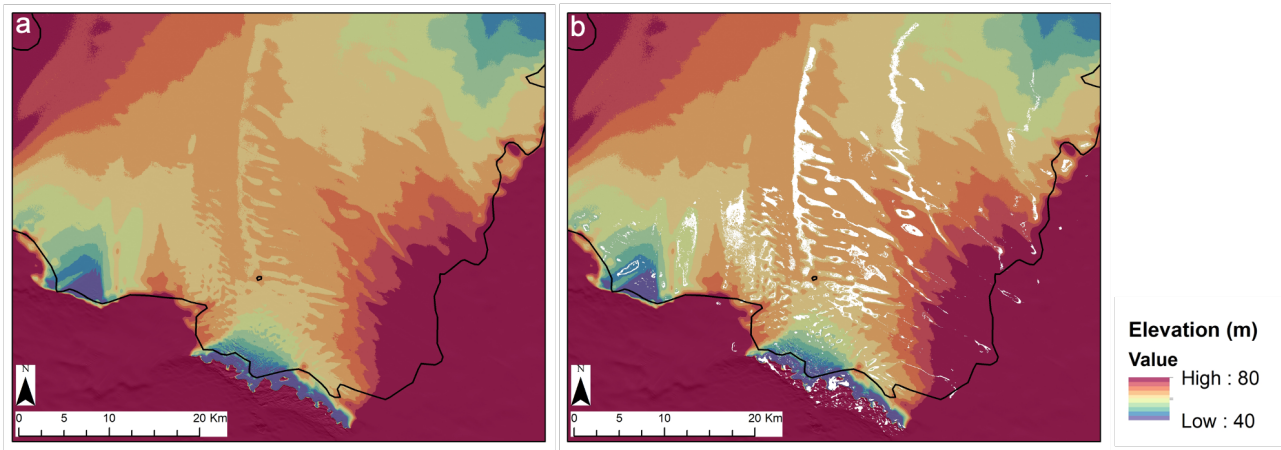
999

1000



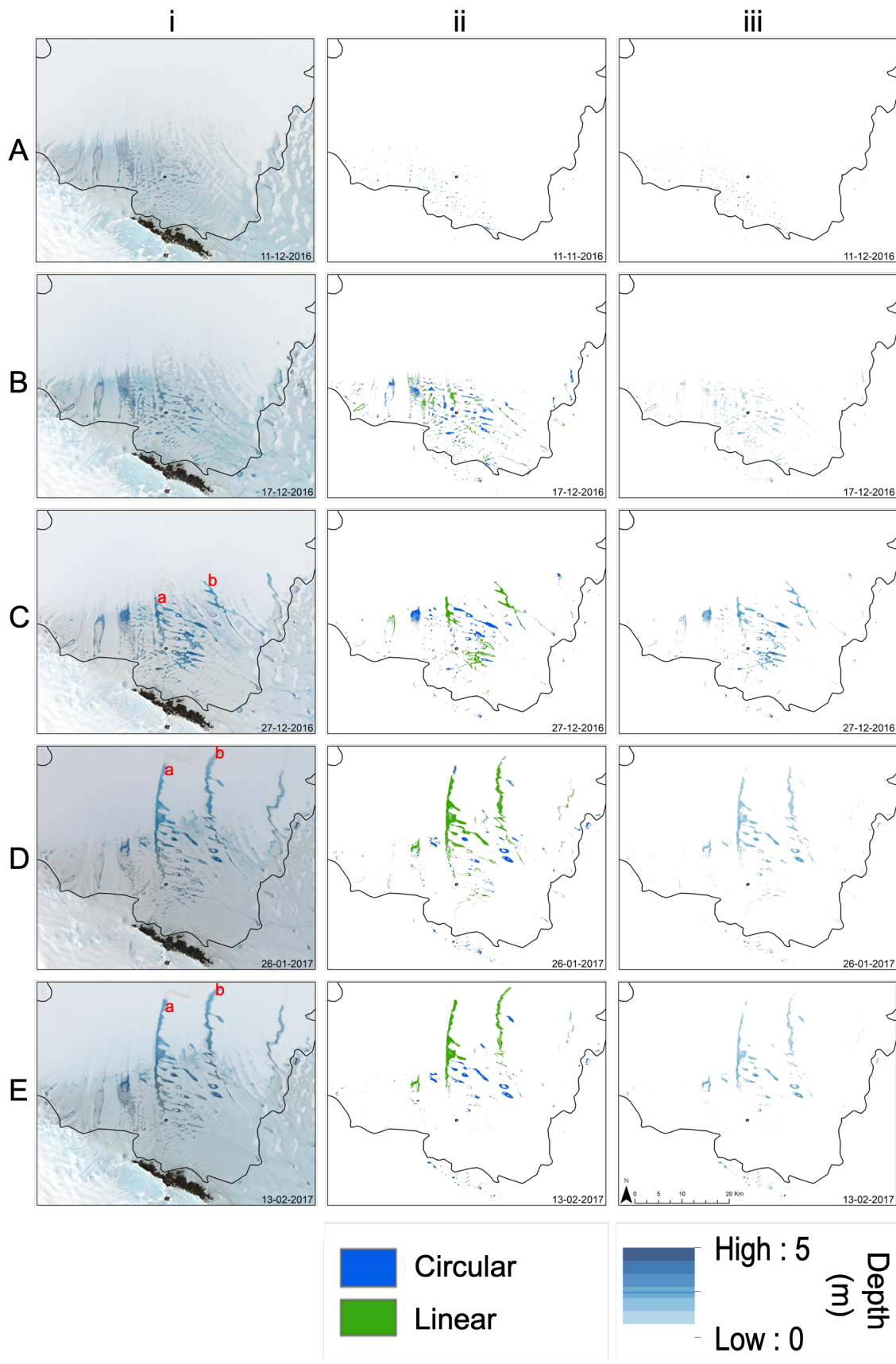
1001
 1002
 1003
 1004
 1005
 1006
 1007
 1008
 1009

Figure 3: Solidity thresholds applied to water bodies identified on the Nivlisen Ice Shelf. The subset Sentinel-2 image is from the 26th January 2017, and the red box indicates the area shown in panels a-d. a) shows this area as an RGB, b) shows the water bodies identified and separated into linear or circular water bodies using a threshold of 0.42, c) a threshold of 0.45, and d) a threshold of 0.49.



1010
 1011
 1012
 1013
 1014
 1015
 1016

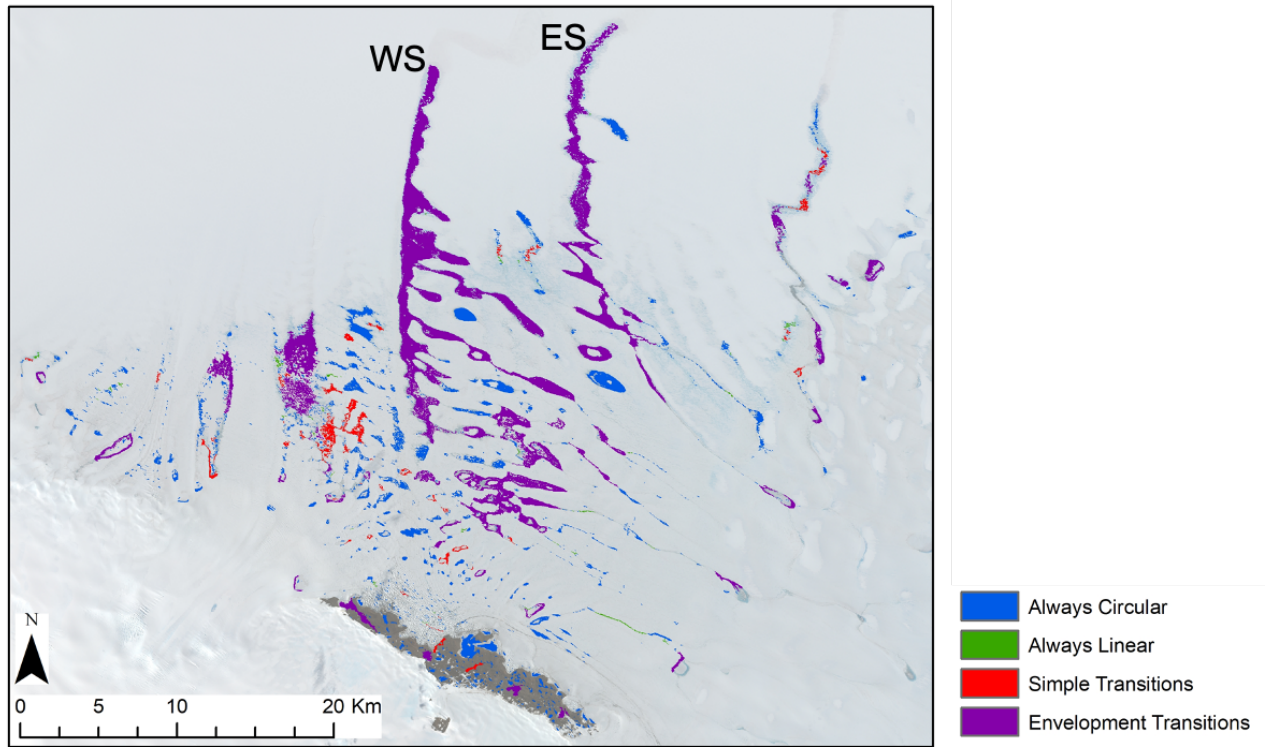
Figure 4: REMA DEM data for the Nivlisen Ice Shelf. a) the DEM; and b) overlain with the maximum melt extent matrix for the 2016-2017 melt season in white. DEM data sourced from the REMA dataset (Howat et al., 2019).



1017
 1018
 1019
 1020
 1021
 1022

Figure 5: Five of the eleven dates studied in the 2016-2017 melt season (represented by labels A-E), and their corresponding (i) RGB images, (ii) lake and stream area masks, (iii) depth masks. See Fig. S2 for all RGB images, Fig. S3 for all lake and stream area masks and Fig. S4 for all depth masks produced in this study.

1023



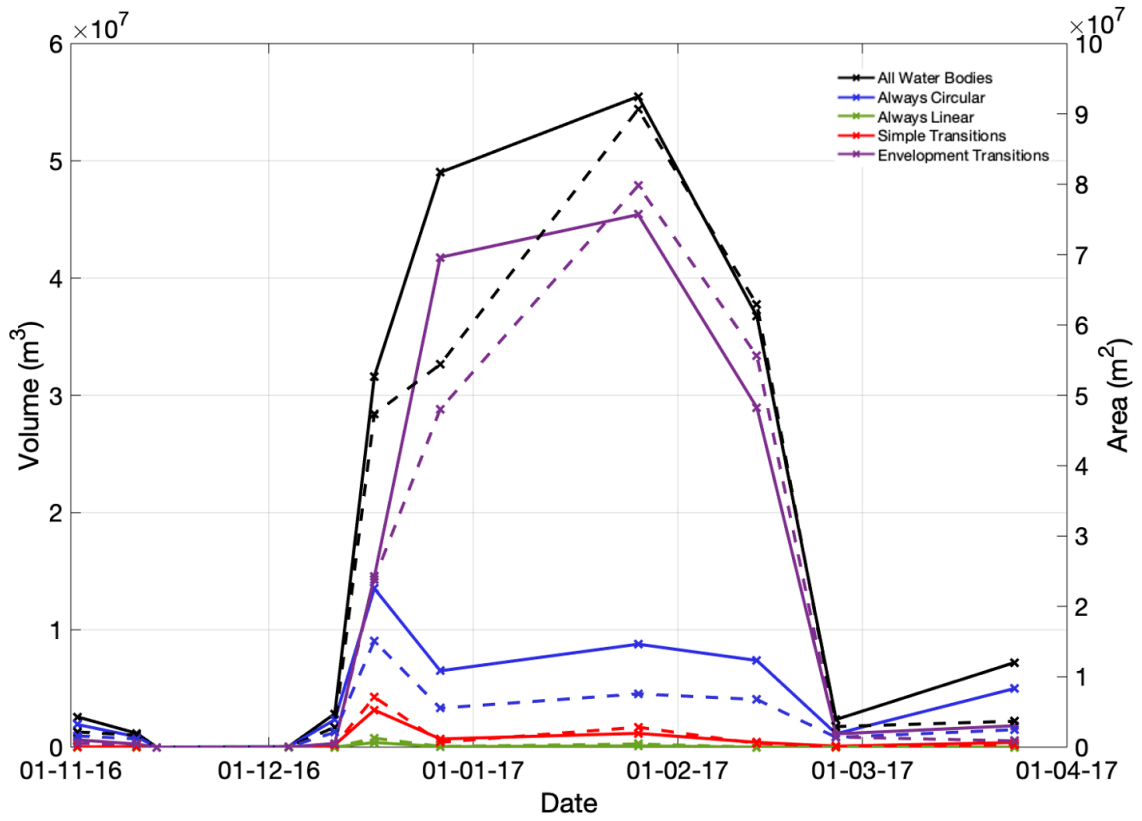
1024

1025 Figure 6: Maximum extent of all identified water bodies on the Nivlisen Ice Shelf for the 2016-2017
1026 melt season, colour coded by water body type. 'WS' donates 'Western System', and 'ES' is
1027 Eastern System. Base image acquired by Sentinel-2 on 26th January 2017.

1028

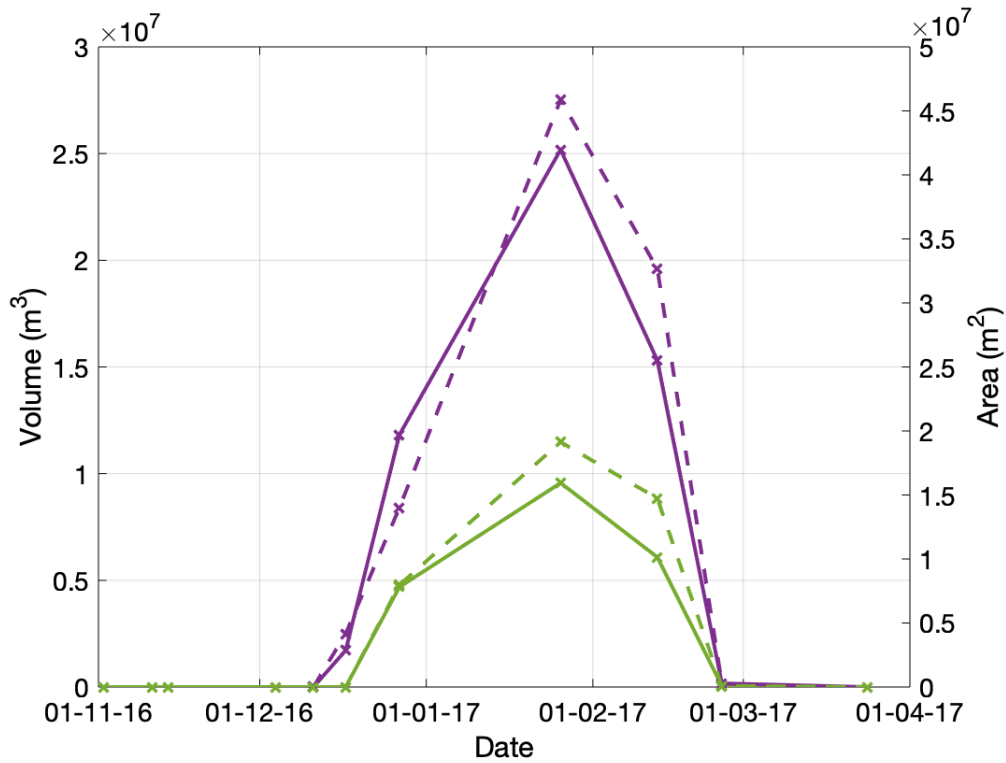
1029

1030



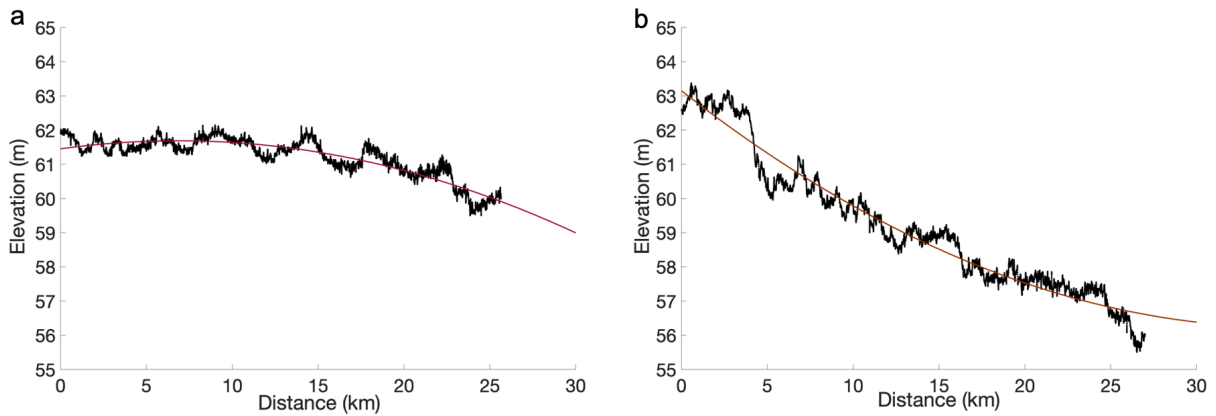
1031
 1032
 1033
 1034
 1035
 1036
 1037
 1038
 1039
 1040

Figure 7: Time series of the total area and volume held in each water body category over the 2016-2017 melt season on the Nivlisen Ice Shelf. Volumes are indicated by the solid lines, and areas by the dashed lines.



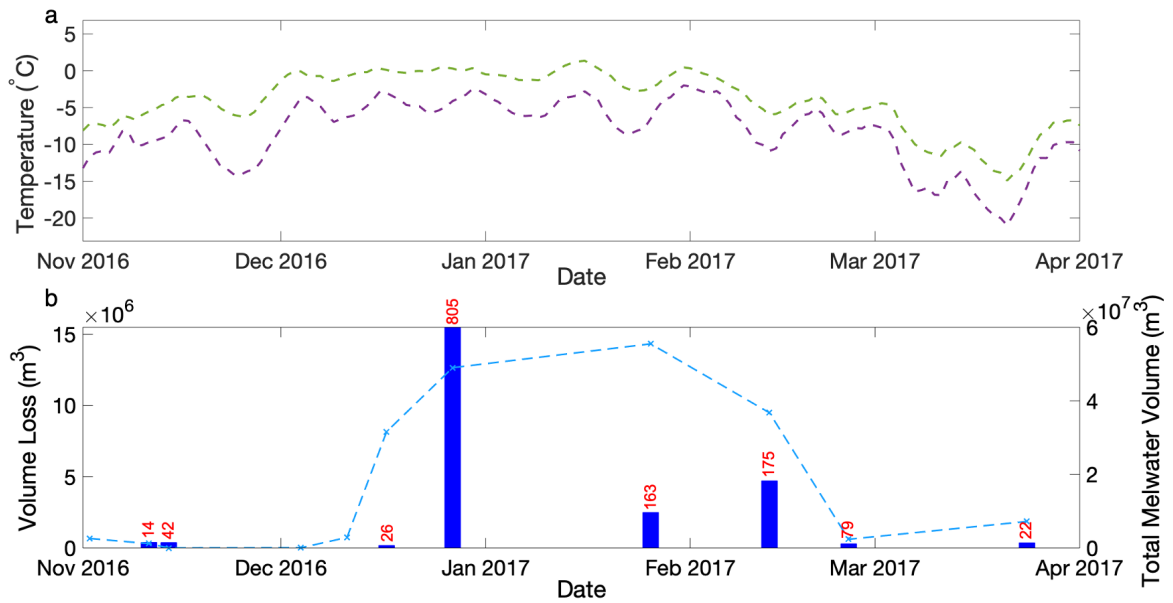
1041
 1042
 1043
 1044
 1045
 1046
 1047

Figure 8: Time series showing the area (dashed line) and volume (solid line) of the WS (purple) and ES (green).



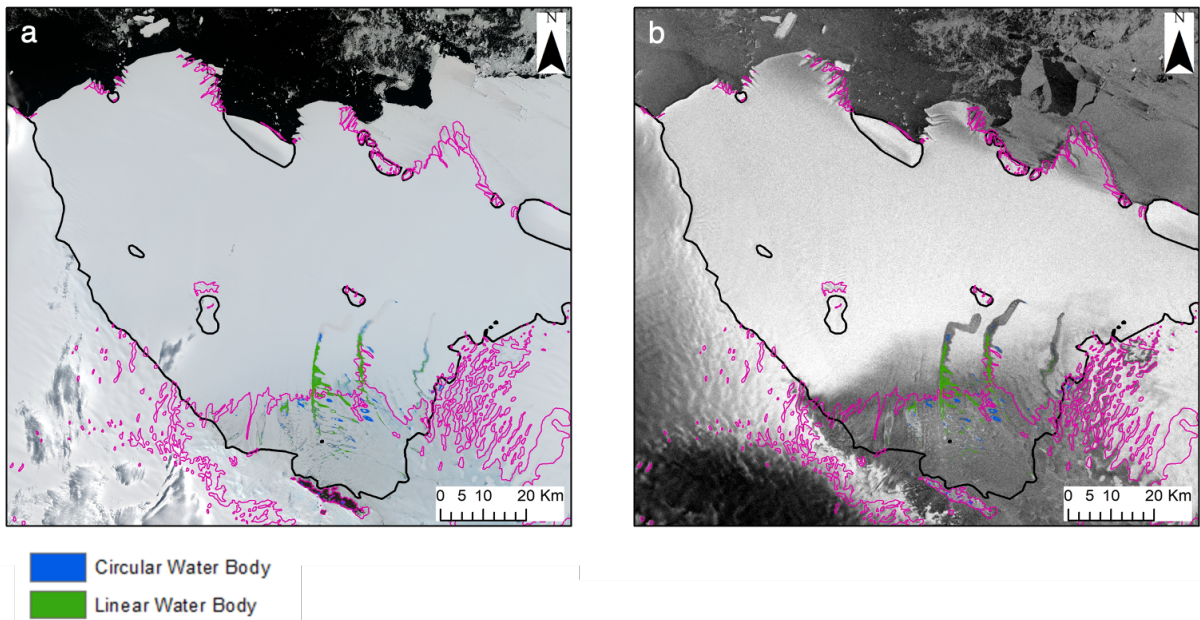
1048
 1049
 1050
 1051
 1052

Figure 9: Elevation profiles for (a) the WS and (b) the ES. Quadratic trendlines are shown in red. Data are extracted from REMA (Howat et al., 2019) and the path of data extraction was guided using the maximum depth matrix of both the WS and ES over the full 2016-2017 melt season (see Fig. S5).



1053
1054
1055
1056
1057
1058
1059
1060
1061
1062

Figure 10: Meteorological context of circular lake loss events: a) The seven day moving average of mean daily (purple line) and daily maximum (green line) near-surface air temperature from the MetUM simulation for the period from November 2016 to April 2017 at the model point immediately to the south of Schirmacheroasen. b) The total volume lost in 'loss events' from water bodies in the 'always circular' category (blue bars) and the total combined water volume (blue line). A loss event is defined as a > 80 % loss in water body volume through either lake drainage or freeze-through. The total number of loss events for each date is indicated above each bar.



1063
1064
1065
1066
1067
1068
1069
1070
1071

Figure 11: Comparison of optical imagery and radar imagery on 26th January 2017; a) is a mosaicked Sentinel-2 image, b) is a Sentinel-1 SAR image. Both a) and b) are overlain with the blue ice extent (pink) and the mapped area of all linear and circular surface water bodies, based on the FASTISH analysis of (a).

1072 Table 1: Total area, total volume, and mean depth of all meltwater bodies on the Nivlisen Ice Shelf
 1073 on various dates in the 2016-2017 melt season.
 1074
 1075

Date	Total Area (m²)	Total Volume (m³)	Mean Depth (m)	Max Depth (m)
2 nd November 2016	2.2 x 10 ⁶	2.6 x 10 ⁶	1.2	2.9
11 th November 2016	1.7 x 10 ⁶	1.2 x 10 ⁶	0.7	2.6
14 th November 2016	0.0	0.0	0.0	0.0
04 th December 2016	4.4 x 10 ⁴	4.0 x 10 ⁴	0.9	3.1
11 th December 2016	2.8 x 10 ⁶	2.8 x 10 ⁶	1.0	3.4
17 th December 2016	4.7 x 10 ⁷	3.2 x 10 ⁷	0.7	3.1
27 th December 2016	5.4 x 10 ⁷	4.9 x 10 ⁷	0.9	4.7
26 th January 2017	9.1 x 10 ⁷	5.5 x 10 ⁷	0.6	3.3
13 th February 2017	6.3 x 10 ⁷	3.7 x 10 ⁷	0.6	4.3
25 th February 2017	2.9 x 10 ⁶	2.4 x 10 ⁶	0.8	3.0
24 th March 2017	3.7 x 10 ⁶	7.2 x 10 ⁶	2.0	5.0

1076
 1077
 1078
 1079
 1080
 1081
 1082
 1083
 1084
 1085
 1086
 1087
 1088
 1089
 1090
 1091
 1092
 1093
 1094
 1095
 1096

Table 2: Maximum Area and Volume for each water body category on the Nivlisen Ice Shelf on various dates in the 2016-2017 melt season.

	Maximum Area (m²)	Maximum Volume (m³)	Date of Maximum Volume	Date of Maximum Area
All Water Bodies	9.1 x 10 ⁷	5.5 x 10 ⁷	26th January 2017	26th January 2017
Always Lakes	1.5 x 10 ⁷	1.4 x 10 ⁷	17th December 2016	17th December 2016
Always Streams	1.3 x 10 ⁶	3.9 x 10 ⁵	17th December 2016	17th December 2016
Simple Transitions	3.2 x 10 ⁶	3.2 x 10 ⁶	17th December 2016	17th December 2016
Envelopment Transitions	8.0 x 10 ⁷	4.5 x 10 ⁷	26th January 2017	26th January 2017

1097

